Active vibration control in specific zones of smart structures

Peng Wang, Anton Korniienko, Xavier Bombois, Manuel Collet, Gérard Scorletti, Ellen Skow, Chuhan Wang, Kévin Colin

Active vibration control in specific zones of smart structures

Peng Wang[a,b], Anton Korniienko[a], Xavier Bombois[a,c], Manuel Collet[b,c], Gerard Scorletti[a], Ellen Skow[a], Chuhan Wang[a], Kevin Colin[a]

[a]*Laboratoire Ampère, UMR CNRS 5005, Ecole Centrale de Lyon, Université de Lyon, Ecully, France, peng.wang@doctorant.ec-lyon.fr, {anton.kornienko, xavier.bombois, gerard.scorletti}@ec-lyon.fr, ellen.skow@gmail.com, chuhan.wang@ecl15.ec-lyon.fr, kevin.colin@ec-lyon.fr*
[b]*LTDS UMR CNRS 5513, Ecole Centrale de Lyon, Université de Lyon, Ecully, France, manuel.collet@ec-lyon.fr*
[c]*Centre National de la Recherche Scientifique (CNRS), France*

Abstract

Smart structures are light structures with integrated sensing and actuating capabilities (smart materials). In this paper, the use of such smart materials for active vibration control is considered, in the case where the vibration covers a large frequency band and the vibration has to be reduced in a region where neither actuation nor sensing is possible. An accurate model combining physical and data-based modeling is developed. A multi-variable H_∞ controller achieving the desired control objective and taking into account the robustness issues is computed. The validity of the proposed approach is verified on an experimental setup.

Keywords: active vibration control, beam-piezo system, vibration energy, MIMO feedback controller, model reduction, H_∞ control, robust stability, grey-box identification

1. Introduction

Lighter structures (generally made of composite materials, aluminum, ...) are increasingly used in many industrial domains (aerospace industry, auto industry, manufacturing industry, etc.). However, such light structures are generally less rigid, so they are more likely to present excessive vibration problems. Consequently, effectively controlling the vibrations in such light structures is an objective of crucial economic importance. This led to the developments of new smart structures with integrated sensing and actuating capabilities (generally realized with piezoelectric transducers due to their high precision and performance [1]). These smart materials/structures allow the development of both passive and active vibration control strategies. Due to the large vibrations in light structures, an active vibration control strategy will generally preferred since this strategy allows a stronger reduction rate.

Active vibration control of flexible structures is a topic that has known a large interest in the literature. In this paper, we extend this literature by considering the situation where the vibration must be rejected in a specific location of the structure where piezoelectric transducers cannot be placed. Such specific zones could e.g. be the location of an antenna on an aircraft fuselage or the location of the passenger's seat in a car. In this situation, we thus aim at reducing the vibration in this specific zone by only using the measurements in other zones. A second challenge tackled in this paper is the fact that we aim at obtaining an important vibration reduction rate (in the specific zone) for vibrations covering a wide frequency range. We will propose a solution to these two challenges and we will verify the validity of the proposed approach by implementing it on a real setup aiming at representing as much as possible the problem at stake. The experimental setup is composed of a free-free aluminum beam where a number of piezoelectric transducers (PZT) have been patched except in the central zone. This central zone will be the one in which the vibration must be reduced. In the considered setup, vibration with a large frequency band can be induced using the force generated by a vibrator located at one end of the beam. To reduce the effect of this force in the central zone of the beam, we will use the measurements of certain of the PZT used as sensors to decide which voltage has to be applied on another set of PZT used as actuators. The relation between measurement and actuation signals will take the form of a model-based controller implemented in D-Space[1]. It is clear that, due to the configuration of the considered setup, the PZT used as

[1] As opposed to passive vibration control, active vibration control thus requires a certain computational power. However, as already mentioned, the reward is a more important vibration reduction.

sensors and as actuators are necessarily outside the zone where the vibration must be reduced (i.e. the central zone).

Our objective is therefore to determine a feedback controller allowing to significantly reduce the vibration energy in the central zone of the experimental beam when this beam is subject to a force disturbance with a large frequency band. The ability of the control loop to reject such a disturbance is of course limited by the working range of the PZT actuators which is here given by $(600, 3000)\ rad/s$. Consequently, by a disturbance with a large frequency band, we mean a disturbance having a large power spectral density in this particular frequency band which covers eleven resonant modes of the beam. This challenging objective requires the use of modern multivariable control design methods. The first reason for this is that these modern control design methods allow to tackle unmeasured performance variables such as the vibration in the central zone where there is no sensor (see e.g. [2] for an example in another context). Second, as we will show in the sequel, in order to control the eleven resonant modes of the beam, we will need to consider at least two sensors and two actuators i.e. we will have to design a multivariable (MIMO) controller. In the literature on active vibration control, methods have first been developed to design SISO controllers to control one resonant mode with a collocated sensor-actuator pair [1, 3, 4, 5, 6]. To control more resonant modes, techniques have also been developed to combine these SISO controllers in parallel [1, 7]. More recently, modern control design methods such as *LQG* (static feedback), H_2 control and H_∞ control (dynamic feedback) have also been considered to design MIMO controllers to control multiple modes [8, 9, 10, 11, 12, 13, 14, 15, 16, 17, 18, 19, 20, 21, 22, 23, 24]. However, to our knowledge, this paper is the first one proposing a technique that allows to significantly reduce a vibration covering a frequency range with as many as eleven modes in a zone where there is no actuator and no sensor.

Our technique is based on dynamic H_∞ control [25] and, as all other modern control design techniques, it requires an accurate model of the to-be-controlled system (i.e. the beam). In this paper, we first deduce a simple physical model of the beam and we then tune its parameters using data collected on the system. As shown in [26], there are multiple well developed beam bending models and the electromechanical coupling between the beam and the PZT can be derived by applying finite element techniques [16, 27, 28] using e.g. the commercial software COMSOL [29]. Such a COMSOL approach will be here considered to derive a state-space model relating the system inputs (the disturbance force and the PZT voltages used for actuation) and the system outputs (the PZT voltages used as sensors and the velocities of a number of points in the central zone[2]), together with a first estimate of the parameters of this model. However, it will be observed that this model is not accurate enough for active vibration control purpose and a more accurate model will be deduced by tuning these parameters using data collected on the experimental setup (grey-box identification, see e.g. [30]). In order to tune the parameters related to these outputs, the vibration velocities in the central zone will be measured using an alternative sensor (i.e. a laser veloci-meter) since no PZT sensors are present in this zone. The obtained identified model will be the one on which the model-based control design approach will be based[3] after a model reduction step that only keeps the modes in the disturbance frequency range[4]. Since both resonances and anti-resonances are important for control, we have used a model reduction technique allowing to obtain a reduced-order model close to the original one both at the resonances and at the anti-resonances. We have recently introduced this technique (see [31]) and its use on a real application is another contribution of this paper.

In addition to the care taken for this model reduction, the H_∞ control paradigm allows to explicitly take into account the modeling error induced by this model reduction step in the design criterion (to guarantee that the controller designed with the reduced-order model also stabilizes the original model). This is one of the main reasons why the H_∞ paradigm is chosen here. This choice is in fact made possible since we also show that, in the case of resonating systems, the main control objective (i.e. minimizing the vibration energy, an objective which is thus more related to the H_2 norm) can also easily be formulated as an H_∞ criterion.

The effectiveness of our approach will be validated via simulations and via actual tests on the available experimental setup.

The rest of the paper is organized as follows. Section 2 describes the experimental setup and points out the control objective. Section 3 gives an overall explanation of the methodology. The details of the methodology are introduced in Section 4 and Section 5. Section 6 applies this methodology on the experimental benchmark. The conclusions are

[2] These outputs will be used to estimate the vibration energy in the central part of the beam.

[3] The quality of this identified model will be evidenced by the almost perfect match between the performance achieved by the model-based controller on the identified model and its performance on the real-life system.

[4] The model reduction is performed to reduce the complexity of the controller.

given in the last section.

Notations: Let us denote $G_{x\to y}$ and $T_{x\to y}$ respectively the open-loop and closed-loop transfer function from x to y, $\mathcal{S}_u$ the Power Spectrum Density (PSD) of a signal u, $\|G\|_2$, $\|G\|_\infty$ respectively the H_2 norm, the H_∞ norm of an LTI system G, $\overline{\sigma}(A)$ the maximum singular value of a matrix A, $diag(A_1, A_2, \cdots, A_n)$ a diagonal or block-diagonal matrix with $A_i, i = 1, 2, \cdots, n$ the diagonal terms or blocks, A^T the transpose of a real matrix A, and A^* the conjugate transpose of a complex matrix A.

2. Experimental setup and control objectives

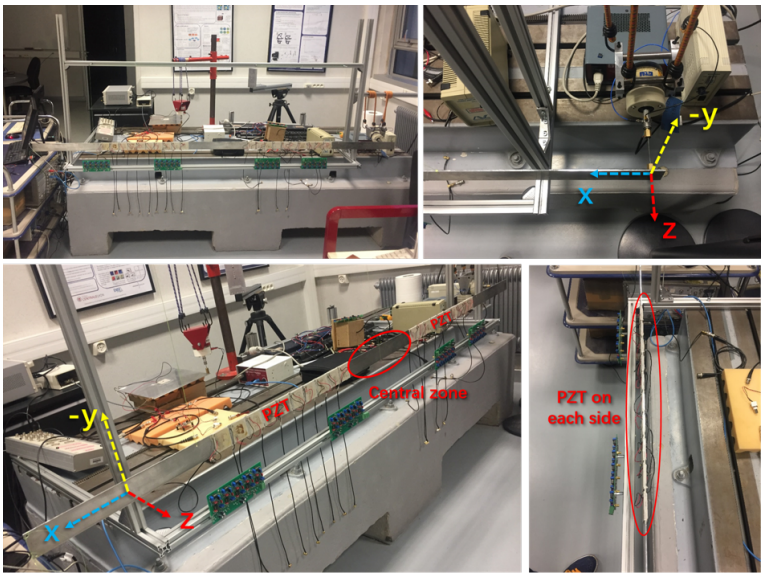

Fig. 1. Pictures of the setup: a general view (top left), the shaker (top right), the central zone and the PZT locations (bottom left), the PZT pairs (bottom right)

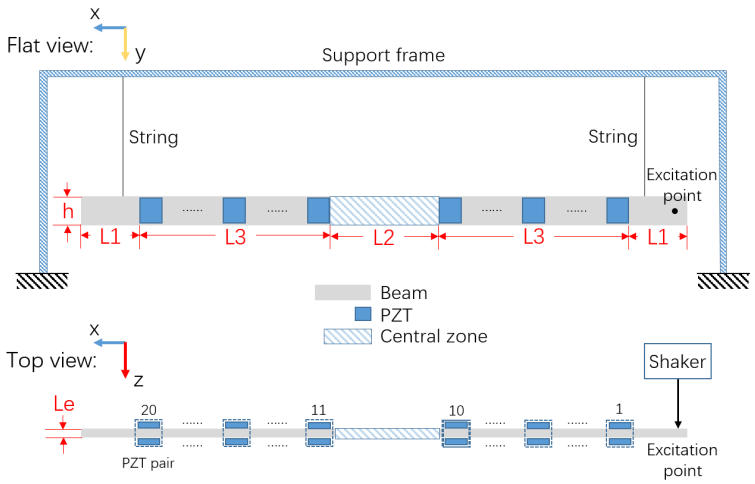

Fig. 2. Schematic diagram of the setup: flat view (top figure); top view (bottom figure)

Fig. 1 shows different pictures of the setup while Fig. 2 gives a schematic description. As already mentioned, the setup is composed of a beam, horizontally hanged on a support frame by two strings to simulate a free-free condition.

A number of PZT are pasted on each side of the beam (in the xy-plane), but not in its central zone which is, as already mentioned, the zone where the vibration energy has to be attenuated. Two PZT at the same location but on different sides form a PZT pair. To distinguish the different pairs, they are numbered from 1 to 20 (See Fig. 2). All dimensions and material properties are summarized in Table 1.

A shaker generates a force disturbance along the z-axis at the right end of the beam. We will only focus on the bending modes along the z-axis. Fig. 3 gives a schematic view of the to-be-designed control system. In this figure, f represents the disturbance force applied by the shaker and the (digital) controller takes as input the sensor voltages V_s of a number of PZT pairs (that have been sampled after passing through an anti-aliasing filter) and delivers as output the voltages V_a to be applied at a number of other PZT pairs (through an amplifier). These (amplified) voltages V_a on the piezo-actuators will have to induce a force whose effect is to counteract the structural vibration (especially) in the central zone. This will in turn imply that, when the controller is active, the transfer function between the disturbance force and the velocities at different points in the central zone will have (much) less pronounced resonance peaks in the frequency range of the force disturbance.

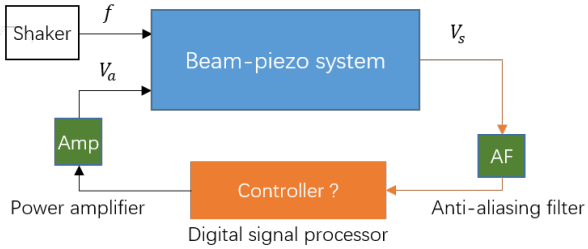

Fig. 3. Block diagram of the controlled system

Table 1: Setup dimensions

Property	**Value**	**Property**	**Value**
Beam density (Aluminum), ρ	$2720\,kg/m^3$	PZT material type	FerroPerm Pz26
Beam total length, L	$2.5\,m$	PZT dimensions	$0.05m \times 0.05m \times 0.0005m$
Beam ends, L1	$0.45\,m$	Distance between PZT	$0.01\,m$
Beam center, L2	$0.42\,m$	Maximum voltage for PZT (guideline)	$200\,VAC/mm$
Beam middle with PZT, L3	$0.59\,m$	Cross-section area of beam, A_S	$159\,mm^2$
Beam hight, h	$0.053\,m$	Young's modulus (Aluminum), Y_{ang}	$69\,GPa$
Beam thickness, Le	$0.003\,m$	Internal resistance of DSpace ADC channel, y_i	$\approx 1\,M\Omega$

As mentioned in the introduction, the disturbance f will here cover the whole working range of the PZT actuators. In the experimental setup, the PZT are of the type Pz26 (see Table 1) whose working range is approximately $(600, 3000)\ rad/s$ which covers 11 vibration modes of the experimental beam. In order to attenuate a vibration over such a large frequency band, we show in Appendix A that we need at least two sensors and two actuators (a SISO controller is therefore not sufficient). In Appendix A, we also show that an appropriate choice for these two actuators and these two sensors is to select the 10^{th} and 16^{th} PZT pairs as actuators, the 5^{th} and 11^{th} PZT pairs as sensors (see Fig. 4 for the location of these PZT pairs).

To sum up, the main objective is to design a 2×2 feedback controller that reduces the vibration energy in the central zone of the beam with respect to a force disturbance which has a large PSD in $(\omega_{low}, \omega_{up}) \triangleq (600, 3000)\ rad/s$. To ensure a good feasibility of the implementation, the order of the controller should be relatively low, which implies that a low-order model containing only the modes in $(600, 3000)\ rad/s$ should be used to compute the controller. As mentioned in the introduction, a grey-box approach will be used to obtain the model of the beam-piezo system and this model (called the full-order model in the sequel) will also contain modes outside $(600, 3000)\ rad/s$. A a consequence, the model order will be reduced and the controller will be designed based on this reduced-order model. This introduces the requirement that the controller remains stable when applied to the full-order model (hence avoiding the so-called spill-over problem). In addition, the controller should have reasonably high magnitude in $(600, 3000)\ rad/s$ to ensure

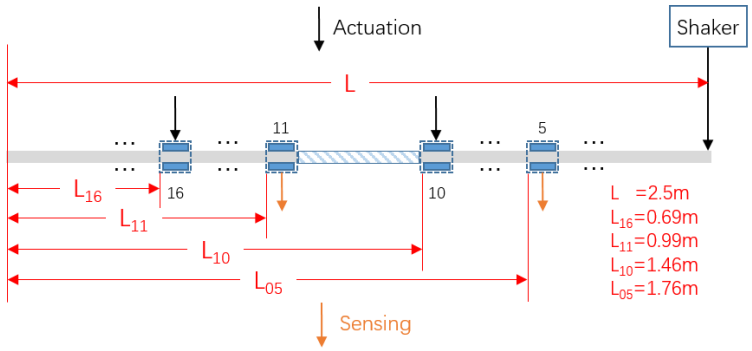

Fig. 4. Actuators and sensors that are chosen to control the system

a high vibration reduction rate while relatively low magnitude outside $(600, 3000)\ rad/s$ to limit energy consumption. For the same reason, one should also take care that sensor/measurement noise (usually located in high frequencies) has limited effect on the control input.

3. Design methodology

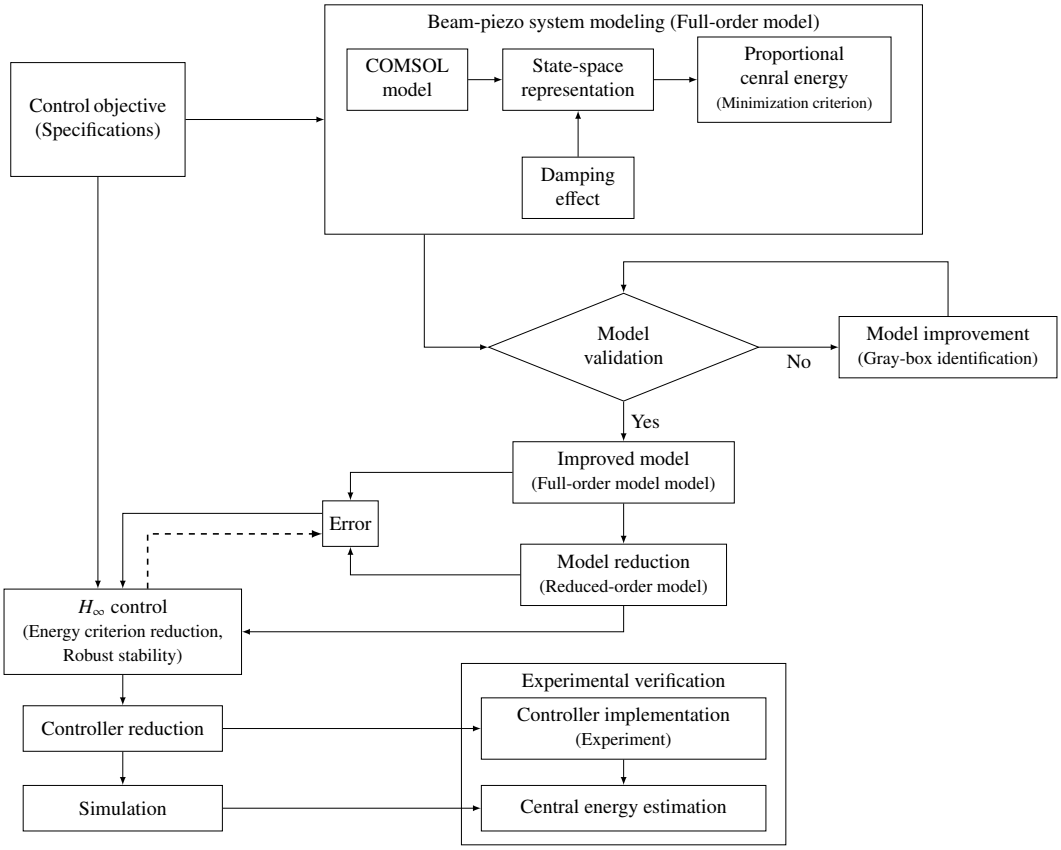

Fig. 5. Methodology

A general overview of the methodology is given in Fig. 5 and each step will be detailed in the following sections. As mentioned in the introduction, the model structure of the beam-piezo system is derived using the commercial

software COMSOL. Since only a finite number of modes can be tackled by COMSOL, the resulting model is a state-space model that is only valid up to a certain user-chosen frequency which is here chosen slightly larger than the maximal frequency of the disturbance i.e. 3000 rad/s. In this state-space model, the output vector is not only made up of the voltages at the two PZT pairs selected as sensors, but also of the (vibration) velocities at a number of locations in the central zone. An expression for the vibration energy in the central zone can indeed be derived from these velocities. Then, the model parameters, for which COMSOL gives a rough initial estimate, are tuned using grey-box identification in order to obtain a model with better accuracy[5], yielding the so-called full-order model of the system. This (full-order) model covers a frequency range that is larger than the frequency range of interest (i.e. $(600, 3000)$ rad/s). A model reduction method is therefore proposed and applied to obtain a reduced-order model that is close to the full-order model in the frequency range of interest. The reduced-order model is then used to design the controller using an H_∞ control design procedure. This control design procedure aims at minimizing the vibration energy in the central zone while keeping the control efforts in acceptable proportion and ensuring that the designed controller will stabilize the full-order model. This last objective is tackled by considering the error between the full-order model and the reduced-order model as an uncertainty. Finally, for the ease of implementation, the obtained controller is reduced without degrading the performance.

4. Modeling

4.1. State-space modeling of the beam-piezo system

Our physical model is based on the following assumptions. First, we only consider the vibration in the z-direction and we will assume that the beam is homogeneous, transverse isotropic and elastic. The effect of bending moments and of lateral displacements will be taken into account in the model, but shear deformation and rotational inertia will be neglected. As discussed before, the boundary condition being free-free, there will be no bending moments or shear forces at both ends of the beam. Note finally that the vibration is generated by a force disturbance applied at one end of the beam as shown in Fig. 2. Based on these assumptions and observations, finite element modeling is performed and leads to a coupling equation (or governing equation) that describes the beam dynamics and the electromechanical coupling between the beam and the PZT [16, 32]. The commercial software COMSOL allows us to derive an expression of this governing equation reflecting the first N resonant modes. In our case, N will be chosen in such a way that the frequency ω_N of this N^{th} mode is slightly larger than the maximal frequency $\omega_{up} = 3000$ rad/s in the frequency band of the disturbance.

4.1.1. Governing equation deduced with COMSOL

The expression of the governing equation up to the N^{th} mode derived via COMSOL can be expressed as follows (see Appendix B for more details). Note that, in the expression below, we have added damping effects, effects that are neglected by COMSOL. To keep the model structure as simple as possible, these damping effects are modeled by two constants κ_a and κ_s. As we will see in the sequel, such a simple model will indeed be sufficient to represent the dynamics of the system.

$$M_{mode} \cdot \ddot{\eta}(t) + (\kappa_a M_{mode} + \kappa_s K_{mode}) \cdot \dot{\eta}(t) + K_{mode} \cdot \eta(t) + E_a \cdot V_a(t) + E_s \cdot V_s(t) = F \cdot f(t), \tag{1}$$

$$-E_s^T \cdot \eta(t) + R_s \cdot V_s(t) = Q_s(t). \tag{2}$$

with $M_{mode} \in \mathbb{R}^{N \times N}$ the normalized mass matrix (which is equal to the identity), $K_{mode} = diag(\omega_1^2, \omega_2^2, \cdots, \omega_N^2)$ the stiffness matrix with ω_i the frequency of the i^{th} mode, $R_s = diag(r_{s_1}, r_{s_2}, \cdots, r_{s_{N_s}})$ the capacity matrix (r_{s_j} is the capacity of the j^{th} PZT sensor and N_s the number of PZT sensors[6]). The matrices E_a and E_s describe the electromechanical coupling between the beam and the PZT actuators and sensors. In addition, the term $F \cdot f(t)$ represents the effect of the external force $f(t)$ on each of the mode and, as introduced before, $V_a(t)$ and $V_s(t)$ are the voltages on the PZT used,

[5] A grey-box identification approach is here preferred over a black-box approach to keep the model order low.

[6] $N_s = 2$ in our case

respectively, as actuators and sensors. The variable $Q_s(t)$ is a vector containing the electrical charge on the PZT used as sensors. By Ohm's law, Q_s (or in fact its derivative) is related to V_s as:

$$\dot{Q}_s(t) = -Y_s \cdot V_s(t) \tag{3}$$

where $Y_s = diag(y_{s_1}, y_{s_2}, \cdots, y_{s_{N_s}})$ is the impedance matrix (y_{s_j} is the impedance of the j^{th} PZT sensor).

The vector $\eta(t) = [\eta_1(t), \eta_2(t), \cdots, \eta_N(t)]^T$ in (1) contains the modal coordinates $\eta_i(t)$ ($i = 1...N$) of the first N modes. According to the modal superposition principle, using these modal coordinates, the displacement $z(x,t)$ in the z-direction at position x (we assume that this displacement is constant along the y-axis) can be approximated[7] as follows

$$z(x,t) \approx \sum_{j=1}^{N} \bar{\varphi}_j(x) \cdot \eta_j(t)$$

where $\bar{\varphi}_j(x)$ is the mode shape corresponding to the j^{th} mode at position x (the function $\bar{\varphi}_j(x)$ can also be derived via COMSOL). The above relation allows us to compute the vibration velocity $v(x,t)$ for any location on the beam (and thus also in the central zone):

$$v(x,t) = \dot{z}(x,t) \approx \sum_{j=1}^{N} \bar{\varphi}_j(x) \cdot \dot{\eta}_j(t) = \varphi(x) \cdot \dot{\eta}(t)$$

where $\varphi(x) = [\bar{\varphi}_1(x), \bar{\varphi}_2(x), \cdots, \bar{\varphi}_N(x)]$.

The above equation can be used to determine the velocities v_{node_i} at N_z locations (nodes) x_i ($i = 1...N_z$) equally distributed in the central zone of the beam i.e. $v_{node_i} = \varphi_{node_i} \cdot \dot{\eta}(t)$ ($\varphi_{node_i} = \varphi(x_i)$). These velocities will allow us to estimate the vibration energy in the central zone.

We can now regroup the above equations in the following state-space model having f and V_a as inputs, V_s and $v_{node} = [v_{node_1}(t), v_{node_2}(t), \cdots, v_{node_{N_z}}(t)]^T$ as outputs and $x(t) = [\eta(t), \dot{\eta}(t), V_s(t)]^T$ as state vector:

$$\begin{cases} \dot{x}(t) = A \cdot x(t) + B_f \cdot f(t) + B_a \cdot V_a(t) \\ v_{node}(t) = C_e \cdot x(t) \\ V_s(t) = C_s \cdot x(t) \end{cases}, \; A = \begin{bmatrix} 0 & I & 0 \\ -K_{mode} & -\kappa_a I - \kappa_s K_{mode} & -E_s \\ 0 & R_s^{-1} \cdot E_s^T & -R_s^{-1} \cdot Y_s \end{bmatrix}, \; B_a = \begin{bmatrix} 0 \\ -E_a \\ 0 \end{bmatrix}, \; B_f = \begin{bmatrix} 0 \\ F \\ 0 \end{bmatrix} \tag{4}$$

$$C_s = \begin{bmatrix} 0 & 0 & I \end{bmatrix}, \; C_e = \varphi_{node} \cdot \begin{bmatrix} 0 & I & 0 \end{bmatrix}, \; \varphi_{node} = [\varphi_{node_1}^T, \varphi_{node_2}^T, \cdots, \varphi_{node_{N_z}}^T]^T$$

For further reference, let us introduce the notation $G^{full}(s)$ for the transfer function matrix relating the inputs and outputs of the above model:

$$\begin{bmatrix} v_{node}(s) \\ V_s(s) \end{bmatrix} = G^{full}(s) \begin{bmatrix} f(s) \\ V_a(s) \end{bmatrix} = \left[\begin{array}{c|c} G^{full}_{f \to v_{node}} & G^{full}_{V_a \to v_{node}} \\ \hline G^{full}_{f \to V_s} & G^{full}_{V_a \to V_s} \end{array}\right] \begin{bmatrix} f(s) \\ V_a(s) \end{bmatrix} \tag{5}$$

An expression for $G^{full}(s)$ can easily be derived by applying the Laplace transform on the state-space model (4).

It is important to note that COMSOL provides us with a first estimate for all parameters[8] in the state-space model (4). In Section 4.2, we will nevertheless show that the values of some of these parameters will have to be refined using data collected on the system for the model described by the above equations to be a good representation of the actual dynamics of the system.

[7] The approximation is due to the truncation of the higher modes.

[8] Note that first estimates for κ_a, κ_s and Y_s are in fact not determined by COMSOL, but can instead be derived using measurement devices (for Y_s) and the half-power method [33] (for κ_a, κ_s).

4.1.2. Determination of the vibration energy in the central zone

Before presenting our approach to refine the parameters of the model, let us show how we can derive an expression for the vibration energy in the central zone. Such an expression is important since this central energy has to be minimized by the to-be-designed feedback controller. The central energy $E_{cent}(t)$ at time t is given by:

$$E_{cent}(t) = \frac{1}{2}\rho S \int_{L_1}^{L_2} v(x,t)^2 \, dx \tag{6}$$

where (L_1, L_2) is the location of the central zone, ρ the beam density and S the intersection area. If we assume a steady-state situation, the average central energy over time is given by:

$$\overline{E_{cent}} = \frac{1}{2}\rho S \lim_{T\to\infty} \frac{1}{T} \int_0^T \left(\int_{L_1}^{L_2} v(x,t)^2 \, dx \right) dt \tag{7}$$

Using the vector v_{node} introduced in the previous subsection, we have the following integral approximation:

$$\int_{L_1}^{L_2} v(x,t)^2 dx \approx v_{node}(t)^T \cdot v_{node}(t) \cdot \Delta x, \tag{8}$$

where Δx denotes the distance between two nodes. Let us now define the average proportional central energy $\overline{E^p_{cent}}$ as follows:

$$\overline{E^p_{cent}} = \lim_{T\to\infty} \frac{1}{T} \int_0^T v_{node}(t)^T \cdot v_{node}(t) \cdot dt \tag{9}$$

It is clear that $\overline{E_{cent}}$ and $\overline{E^p_{cent}}$ are (approximately) proportional. Thus, we can also conclude that reducing $\overline{E^p_{cent}}$ implies reducing $\overline{E_{cent}}$. Moreover, if we define the PSD of the disturbance f as $|L_f(j\omega)|^2$ with a transfer function $L_f(s)$, we can use Parseval's theorem to give the following computable expression of $\overline{E^p_{cent}}$:

$$\begin{aligned} \overline{E^p_{cent}} &= \frac{1}{2\pi} \int_{-\infty}^{+\infty} H^*(j\omega) H(j\omega) |L_f(j\omega)|^2 \, d\omega \\ &= \left\| H(s) L_f(s) \right\|_2^2 \end{aligned} \tag{10}$$

where $H(s)$ is the vector of transfer functions relating the force f and the vector v_{node}. In the open-loop situation, $H(s)$ is equal to $G^{full}_{f\to v_{node}}(s)$ (see Eq. (5)). In the closed-loop situation i.e. when the controller $K(s)$ is active, $H(s)$ is then equal to the closed-loop transfer vector between f and v_{node} that we will denote by $T^{full}_{f\to v_{node}}(s)$. This closed-loop transfer vector can be easily determined by adding the relation[9] $V_a(s) = K(s)V_s(s)$ to Eq. (5), yielding: $v_{node}(s) = T^{full}_{f\to v_{node}} f(s)$.

4.2. Model validation and improvement

In Section 4.1, a physical model has been derived for the to-be-controlled system under the form of the state-space model (4) relating the system inputs (the disturbance force $f(t)$ and the actuator vector $V_a(t)$) and the system outputs (the sensor vector $V_s(t)$ and the vector $v_{node}(t)$ containing the speed of displacements at a number of points in the central zone). As already mentioned, this physical model is parameterized by a number of physical parameters for which a first estimate can be derived using COMSOL or classical tests. This first estimate is very accurate for K_{mode}, R_s and Y_s. However, this first estimate is much cruder for the rest of the parameters: κ_a, κ_s, E_a, E_s, F and φ_{node}. For further reference, these remaining parameters are gathered in a vector θ and we will denote by θ_{init} its first estimate. The vector θ will be further divided in three terms $\theta^T = (\theta_1^T, \theta_2^T, \theta_3^T)$: θ_1 contains the scalar parameters κ_a, κ_s and the elements of the matrices E_a and E_s, θ_2 contains the elements of the vector F and θ_3 contains the elements in the matrix φ_{node}. System identification will be used to obtain a more accurate estimate of the unknown parameter vector

[9] Note that, in Section 5, the notation $K(s)$ will in fact be used for the controller before amplification.

θ, denoted $\theta_{id}^T = (\theta_{1,id}^T, \theta_{2,id}^T, \theta_{3,id}^T)$. For this purpose, experiments will be performed on the experimental setup and the corresponding input-output data will be collected. Due to the particular structure of the physical model (4), three different types of experiments will be performed and this will allow one to successively deduce accurate estimates for θ_1, θ_2 and finally θ_3. These separate identification experiments have the advantage to reduce the complexity of the identification criteria.

Experiment 1. Let us first notice that, when f is forced to zero, the relation between V_a and V_s is only function of the parameter vector θ_1 (see Eq. (4)). An experiment is performed on the experimental setup with $f = 0$ and with independent white noise signals applied to both actuators (i.e. V_a). Denote $V_{s,m_1}(t = nT_s)$ with $n = 1, 2, \cdots, N_d$ the corresponding output voltages measured at a sampling rate T_s after the application of an anti-aliasing filter. A more accurate estimate of θ_1 can then be deduced by solving the following output error identification criterion:

$$\theta_{1,id} = \arg\min_{\theta_1} \frac{1}{N_d} \sum_{n=1}^{N_d} \left(V_{s,m_1}(nT_s) - \hat{V}_s(nT_s, \theta_1)\right)^T \left(V_{s,m_1}(nT_s) - \hat{V}_s(nT_s, \theta_1)\right),$$

where $\hat{V}_s(nT_s, \theta_1)$ is the output voltage $V_s(t)$ predicted by Eq. (4) at $t = nT_s$ for an arbitrary value of θ_1 and for the input $V_a(t)$ applied during the experiment ($f(t) = 0$).

This criterion is of course nonlinear in θ_1. Consequently, the determination of $\theta_{1,id}$ requires an appropriate initialization which in our case can be taken equal to the first estimate of θ_1, i.e. $\theta_{1,init}$.

Experiment 2. Notice now that, when $V_a = 0$, the relation between f and V_s is function of θ_1 and θ_2. Since an accurate estimate of θ_1 has been determined in the first experiment (i.e. $\theta_{1,id}$), the relation between f and V_s can be reduced to a model which is only function of θ_2. An experiment is therefore performed on the experimental setup with $V_a = 0$ and with a force corresponding to a white noise signal. Denote $V_{s,m_2}(t = nT_s)$ with $n = 1, 2, \cdots, N_d$ the corresponding output voltages measured at a sampling rate T_s after the application of an anti-aliasing filter. A more accurate estimate of θ_2 can then be deduced by solving the output error identification criterion:

$$\theta_{2,id} = \arg\min_{\theta_2} \frac{1}{N_d} \sum_{n=1}^{N_d} \left(V_{s,m_2}(nT_s) - \tilde{V}_s(nT_s, \theta_2, \theta_{1,id})\right)^T \left(V_{s,m_2}(nT_s) - \tilde{V}_s(nT_s, \theta_2, \theta_{1,id})\right),$$

where $\tilde{V}_s(nT_s, \theta_2, \theta_{1,id})$ is the output voltage $V_s(t)$ predicted by Eq. (4) at $t = nT_s$ for an arbitrary value of θ_2 and for $\theta_1 = \theta_{1,id}$ and for the applied input force $f(t)$ ($V_a = 0$).

This criterion is of course nonlinear in θ_2, but it can be initialized with the first estimate of θ_2 i.e. $\theta_{2,init}$.

Experiment 3. Notice that the relation between f and v_{node} is function of θ_1, θ_2 and θ_3 and that an accurate estimate of θ_1 and θ_2 has been deduced via Experiments 1 and 2. Consequently, using a similar approach as in Experiment 2, an estimate of θ_3 i.e. $\theta_{3,id}$ can be deduced by applying a white noise signal at the input $f(t)$ ($V_a = 0$) and by measuring $v_{node_i}(t)$ using a laser velocimeter ($i = 1, 2, \cdots, N_z$). The laser velocimeter is necessary to measure $v_{node_i}(t)$ since there is no piezo-patches in the central zone[10]. In fact, since a laser velocimeter has to be used to measure v_{node_i}, the experiment has to be repeated N_z times and each of these N_z experiments allows to deduce a part of $\theta_{3,id}$ (i.e. the part containing the parameters in $\varphi_{node_i}, i = 1, 2, \cdots, N_z$).

The approach presented above allows to derive a model $G^{full}(\theta_{id})$ of the to-be-controlled system that is much more accurate than the model corresponding to θ_{init} (i.e. the model deduced by COMSOL). The improvement will be illustrated in Section 6 by comparing the frequency response of the parametric model $G^{full}(\theta_{id})$ with an accurate non-parametric estimate of this frequency response that can be deduced from a frequency analyzer. An almost perfect match between the frequency analyzer estimate and the frequency response of $G^{full}(\theta_{id})$ will be observed while the frequency response of $G^{full}(\theta_{init})$ is indeed much more different.

Remark. Note that, before proceeding to the identification of the parameter vector in each of these three steps, the collected data can be pre-filtered using a band-pass filter focusing on the frequency band of interest.

[10]The fact that we can refine the parameter vector θ_3 using data collected using this laser velocimeter is the main reason for our choice to use v_{node} as the physical signal to evaluate the central energy. Other approaches such as the one in [34] does indeed not have this advantage.

4.3. Model reduction

In this section, we will present the model reduction technique which will be applied on the (full-order) model $G^{full}(\theta_{id})$ identified in the previous section. The dynamic range of this model is indeed larger than the frequency range of interest $(\omega_{low}, \omega_{up}) = (600, 3000)\ rad/s$. As already mentioned, the objective is to obtain a reduced-order model having a frequency response which is close to the one of $G^{full}(\theta_{id})$ in $(\omega_{low}, \omega_{up})$ and this not only for the resonances, but also for the anti-resonances. Both are indeed important for control as evidenced in [22]. The model reduction approach proposed in this paper consists of two steps.

The first step that we will call Modal Form Truncation (MFT) is an application of the Aggregation Technique [35]. The full-order model is transformed into the so-called modal form or Diagonal Canonical Form [36]. In modal form, the dynamic matrix A is indeed diagonal by block:

$$A = \begin{bmatrix} A_1 & & 0 \\ & A_2 & \\ & & \ddots \\ 0 & & A_n \end{bmatrix}$$

where A_i is either a scalar (for the poles corresponding to the measurement circuit) or a 2×2 matrix (for the poles corresponding to the vibration modes). Consequently, it is rather straightforward to remove those blocks which correspond to the modes outside $(\omega_{low}, \omega_{up})$ and so to reduce the model order. Similar operations can be performed on the other state-space matrices yielding the following reduced-order model for G^{full}:

$$\begin{cases} \dot{x} = A^r \cdot x + B_f^r \cdot f + B_a^r \cdot V_a \\ v_{node} = C_e^r \cdot x \\ V_s = C_s^r \cdot x \end{cases} \tag{11}$$

It is important to note that the truncation involved in this first step generally introduces a mismatch between full-order and reduced-order models around anti-resonance frequencies. Consequently, the second step will adapt the reduced-order model obtained after the first step in order to reduce this mismatch. This is done by considering the relative error between full-order and reduced-order models in the reduction criterion since this definition of the error gives similar weighting to both resonances and anti-resonances [37]. Note that, for simplicity, we will only adapt the part between V_a and V_s in the above model. More precisely, we will determine $C_s^{r,new}$ and $D_s^{r,new}$ in such a way that the following relative error is minimized:

$$\Delta(j\omega) = G^{-1}_{V_a \to V_s}(j\omega)\left(G^{full}_{V_a \to V_s}(j\omega) - G_{V_a \to V_s}(j\omega)\right) \tag{12}$$

where $G^{full}_{V_a \to V_s}$ is the transfer function between V_a and V_s in the full-order model (see Eq. (5)) and $G_{V_a \to V_s}$ is the transfer function between V_a and V_s corresponding to the following state-space model:

$$\begin{cases} \dot{x} = A^r \cdot x + B_a^r \cdot V_a \\ V_s = C_s^{r,new} \cdot x + D_s^{r,new} \cdot V_a \end{cases} \tag{13}$$

where A^r and B_a^r are the same as the ones obtained after the first model reduction step (see Eq. (11)) and where $C_s^{r,new}$ and $D_s^{r,new}$ will be optimized (note that we have added a direct term to the model to increase the degrees of freedom). As already mentioned, the second step thus only focuses on the relative error pertaining to the part of Eq. (11) between V_a and V_s. The main reasons for this are simplicity and the fact that $G_{V_a \to V_s}$ is the part of the model which is directly involved in the closed-loop system. The error at the anti-resonances is indeed only required to be small for the reduced-order model to be a good model for control purpose. Moreover, we only tune the matrices $C_s^{r,new}$ and $D_s^{r,new}$ since we want to improve the behavior at the anti-resonances (which is linked to the state-space matrices C and D) and not the behavior at the resonances (which are linked to the state-space matrix A).

Finally, since only the behavior in the frequency band $(\omega_{low}, \omega_{up})$ is of interest, we will use the following optimization problem to determine $C_s^{r,new}$ and $D_s^{r,new}$:

$$\min_{C_s^{r,new}, D_s^{r,new}} \sup_{\omega \in (\omega_{low}, \omega_{up})} \overline{\sigma}\left(G^{-1}_{V_a \to V_s}(j\omega)(G^{full}_{V_a \to V_s}(j\omega) - G_{V_a \to V_s}(j\omega))\right). \tag{14}$$

As shown in our recent paper [31] (see also Appendix C), this optimization problem can be transformed into a convex optimization problem involving Linear Matrix Inequality (LMI) [38] constraints and can therefore be easily solved.

The reduced-order model after this two-step procedure is thus finally given by the following state-space model, which will be used in the next section to design the controller:

$$\begin{cases} \dot{x} = A^r \cdot x + B_f^r \cdot f + B_a^r \cdot V_a \\ v_{node} = C_e^r \cdot x \\ V_s = C_s^{r,new} \cdot x + D_s^{r,new} \cdot V_a \end{cases} \tag{15}$$

Similarly as in Eq. (5), this reduced-order model can be transformed into a matrix of transfer functions that will be denoted by G. In the next section, we will show how to design the controller based on G. Note that, by construction, the reduced-order model G will typically have low gain outside $(\omega_{low}, \omega_{up})$. See e.g. Fig. 12 for a confirmation of this observation.

5. Controller design via the H_∞ approach

In this section, the H_∞ control approach is first introduced theoretically and then applied to solve our particular active vibration attenuation problem.

5.1. H_∞ control approach

5.1.1. Performance and criterion

Restricting attention to disturbance rejection, the objective of H_∞ control is to design a controller $K(s)$ ($u(s) = K(s)y(s)$) for a system of the type:

$$\begin{bmatrix} q(s) \\ y(s) \end{bmatrix} = \tilde{G}(s) \begin{bmatrix} p(s) \\ u(s) \end{bmatrix} \tag{16}$$

where $u(s) \in \mathbb{C}^{n_u}$ is the (Laplace transform of the) vector of signals generated by the controller and $y(s) \in \mathbb{C}^{n_y}$ the vector containing the sensor measurements used by the controller $K(s)$. In the above system, we have also $p(s) \in \mathbb{C}^{n_p}$ which is a vector containing the to-be-rejected disturbances and $q(s) \in \mathbb{C}^{n_q}$ which is a vector containing the to-be-controlled outputs. It is to be noted that q does not need to be measured (this aspect will be important in our case) Finally, $\tilde{G}(s)$ is a matrix of transfer functions reflecting the dynamics between these signals. In our case, we will have that $u = V_a$, $y = V_s$, p will be made up of the disturbance f and the measurement noise and q will be made up of v_{node} (since we want to reduce the central energy) and V_a (since we want to have limited control efforts). See Section 5.2 for more details.

To define the criterion that will yield the controller $K(s)$, it is important to describe the frequency content of $p(s)$ and the desired frequency content of $q(s)$. For this purpose, let us introduce, for an arbitrary signal x of power spectral density (PSD) $\mathcal{S}_x(\omega)$, the following signal set defined by a stable and inversely stable transfer function $W(s)$:

$$\Omega_W = \left\{ x \middle| \forall \omega,\ \mathcal{S}_x(\omega) \leqslant |W(j\omega)|^2 \right\} \tag{17}$$

Based on this expression, we determine transfer functions W_{p_j} ($j = 1...n_p$) such that each element p_j of p belongs to the set $\Omega_{W_{p_j}}$ and we determine transfer functions W_{q_k} ($k = 1...n_q$) such that, if each element q_k of q belongs to the signal set $\Omega_{W_{q_k}^{-1}}$, the to-be-controlled outputs q satisfy the desired specifications. The objective of H_∞ control is then to determine a controller $K(s)$ that, when applied to the system described by Eq. (16), each element q_k of q will belong to $\Omega_{W_{q_k}^{-1}}$ ($q = 1...n_q$) if each element p_j of p belongs to $\Omega_{W_{p_j}}$ ($j = 1...n_p$). It is to be noted that, in general, we will not need to define all these transfer functions W_{p_j} and W_{q_k}. Simplifications will be used which will generally based on the following interpretation of the H_∞ control problem in term of the loop-shaping of the closed-loop transfer functions

i.e. if a controller satisfying the above objectives is applied to Eq. (16), then the following inequality holds for the closed-loop transfer function $T_{p_j \to q_k}$ between any signal p_j ($j = 1...n_p$) and any signal q_k ($q = 1...n_q$):

$$\forall \omega, \ |T_{p_j \to q_k}(j\omega)| < \frac{1}{|W_{q_k}(j\omega) W_{p_j}(j\omega)|}. \tag{18}$$

We can thus also see the transfer functions W_{p_j} and W_{q_k} as weightings to shape the closed-loop transfer functions. Let us now mathematically formalize the control design problem defined above. For this purpose, let us define the so-called augmented plant $P(s)$:

$$P(s) = diag(W_{q_1}, \cdots, W_{q_{n_q}}, I_{n_y}) \tilde{G}(s) diag(W_{p_1}, \cdots, W_{p_{n_p}}, I_{n_u}). \tag{19}$$

This augmented plant is represented in Fig. 6 where the signals e_j ($j = 1...n_p$) and z_k ($k = 1...n_q$) are fictive signals that all have a PSD smaller or equal to one when p_j belongs to $\Omega_{W_{p_j}}$ ($j = 1...n_p$) and q_k belongs to $\Omega_{W_{q_k}^{-1}}$ ($q = 1...n_q$).

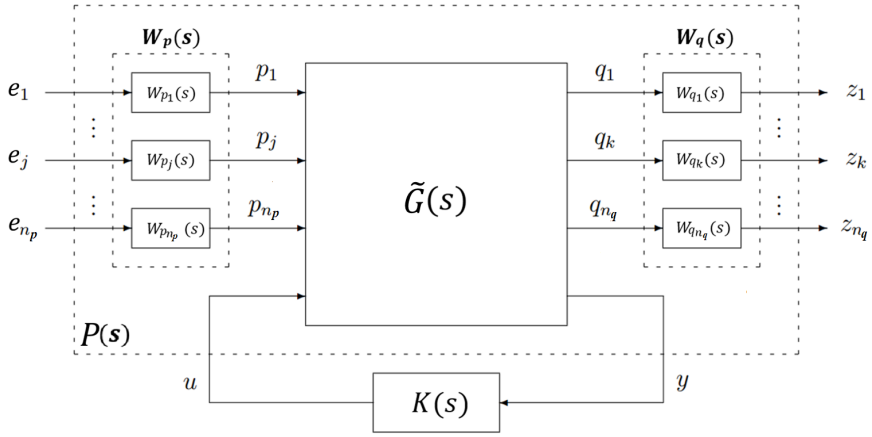

Fig. 6. Standard form of H_∞ synthesis

Denoting $e = [e_1, \cdots, e_{n_p}]^T$ and $z = [z_1, \cdots, z_{n_q}]^T$, the closed-loop system can then be rewritten as:

$$\begin{bmatrix} z(s) \\ y(s) \end{bmatrix} = P(s) \begin{bmatrix} e(s) \\ u(s) \end{bmatrix}, \quad u(s) = K(s) y(s) \tag{20}$$

The transfer function between e and z in Eq. (20) will be denoted $P \star K$ in the sequel ($\star$ is the so-called Redheffer star product [25]). Using Eq. (20), the H_∞ control criterion described above can be mathematically formulated as the problem of determining a stabilizing controller $K(s)$ such that the following condition holds for the smallest possible scalar $\gamma < 1$:

$$\|P(s) \star K(s)\|_\infty < \gamma, \tag{21}$$

where the H_∞ norm of an arbitrary stable LTI system T is defined as:

$$\|T\|_\infty = \sup_\omega \overline{\sigma}(T(j\omega)). \tag{22}$$

Eq. (21) implies that each entry of $P \star K$ has an H_∞ norm smaller than $\gamma < 1$, which in turn implies Eq. (18). Note that the H_∞ controller K designed in this way will have the same order as the augmented plant P.

5.1.2. *A robust stability result*

Before presenting the particular H_∞ control design used for our active vibration problem, let us recall the so-called Weighted Small Gain Theorem [39] which is an important result in robustness analysis and which will be crucial to understand one of the aspects of the chosen H_∞ criterion. For this purpose, let us define the following uncertainty set $\mathbf{\Delta}$ containing stable LTI transfer matrices $\Delta(s)$:

$$\mathbf{\Delta} = \left\{ \Delta(s) \mid \Delta(s) = W_1(s)\hat{\Delta}(s)W_2(s) \text{ with } \left\|\hat{\Delta}\right\|_\infty \leqslant 1 \right\}, \tag{23}$$

with W_1 and W_2 two given stable transfer matrices. Then, for a stable transfer matrix $M_d(s)$, the loop represented in Fig. 7 is stable for all Δ in $\mathbf{\Delta}$ if and only if the following condition holds:

$$\|W_2 M_d W_1\|_\infty < 1. \tag{24}$$

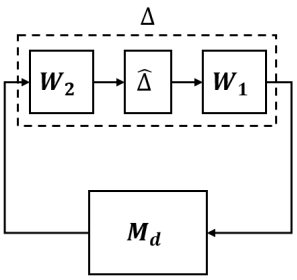

Fig. 7. Weighted Small Gain Theorem (WSGT)

5.2. H_∞ *controller design*

We are now ready to present the H_∞ criterion we will use to tackle our vibration attenuation problem. Let us for this purpose define the augmented system P as shown in Fig. 8. In this figure, G is the reduced-order model obtained from model reduction (see Section 4.3, Eq. (15)), K the to-be-determined controller. This controller generates a signal u that will be applied as voltage V_a to the PZT actuators after an amplification by a factor A_p (power amplifiers) and uses a signal y which is obtained after filtering the PZT sensors by an anti-aliasing filter. The digital conversion[11] mechanism of the anti-aliasing filter is here replaced by the transfer function $F_d(s)$ where Pade Approximation is used to model the introduced delay [40]. Recall that N_a and N_s are respectively the number of PZT actuators and sensors used for control ($N_a = N_s = 2$ in our case).

In Fig. 8, we see also that the vector z (corresponding to the to-be-controlled variables q) is made up of v_{node} and of a weighted version z_u of u and that the vector e (corresponding to the disturbance signals p) is made up of a weighted version e_1 of the disturbance f generated by the shaker, of a weighted version e_2 of the output measurement noise b and a weighted version e_3 of a signal c that will allows us to deal with the modeling error introduced by the model reduction step (see Section 4.3). Finally, W_f, W_b, W_Δ and A_t are weighting functions (under the form of a SISO transfer function for W_Δ and of constants for W_f, W_b and A_t) which have to be determined in order to realize the specifications described at the end of Section 2.

Note that Fig. 8 corresponds to the standard form of H_∞ synthesis (see Fig. 6) with $P(s) = W_q(s)\tilde{G}(s)W_p(s)$ where:

$$\tilde{G}(s) = \begin{bmatrix} I_{N_z} & 0 & 0 & 0 \\ 0 & 0 & 0 & I_{N_a} \\ 0 & F_d(s)I_{N_s} & I_{N_s} & 0 \end{bmatrix} \left[\begin{array}{cc|cc} & & 0 & 0 \\ & \text{G(s)} & 0 & 0 \\ \hline 0 & 0 & I_{N_s} & 0 \\ 0 & 0 & 0 & I_{N_a} \end{array}\right] \begin{bmatrix} 1 & 0 & 0 & 0 \\ 0 & 0 & A_p I_{N_a} & A_p I_{N_a} \\ 0 & I_{N_s} & 0 & 0 \\ 0 & 0 & 0 & I_{N_a} \end{bmatrix},$$

[11] The controller will thus be implemented digitally

$$W_q(s) = \begin{bmatrix} I_{N_z} & 0 \\ 0 & A_t W_\Delta(s) I_{N_a} \end{bmatrix}, \quad W_p(s) = \begin{bmatrix} W_f(s) & 0 & 0 \\ 0 & W_b(s) I_{N_s} & 0 \\ 0 & 0 & \frac{1}{A_t} I_{N_a} \end{bmatrix}.$$

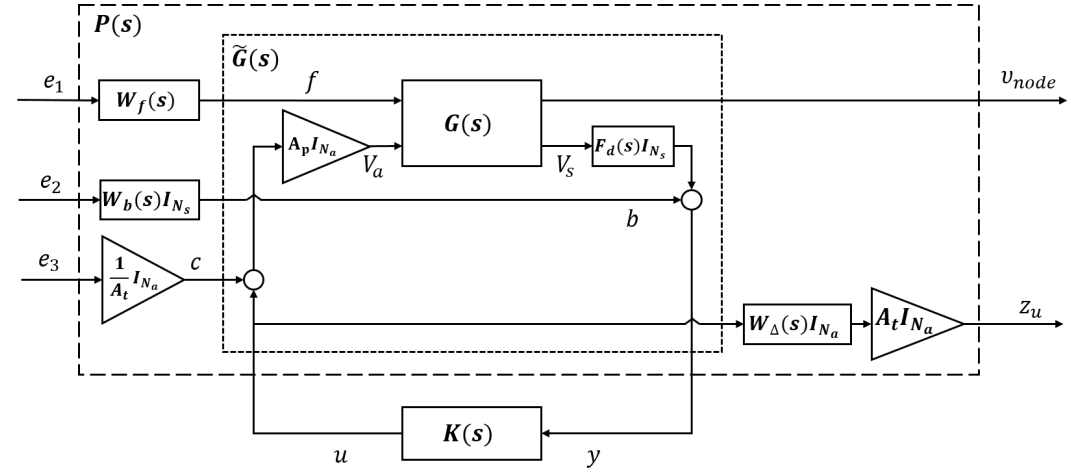

Fig. 8. Block diagram of H_∞ synthesis

Consequently, the controller K determined using H_∞ synthesis will be such that $\|P \star K\|_\infty < \gamma$ holds for the smallest possible $\gamma < 1$. The latter in particular implies:

a. $\|T_{e_1 \to v_{node}}\|_\infty < \gamma < 1$

b. $\|T_{e_3 \to z_u}\|_\infty < \gamma < 1$

c. $\|T_{e_1 \to z_u}\|_\infty < \gamma < 1$ and $\|T_{e_2 \to z_u}\|_\infty < \gamma < 1$

We can now present how we can choose the constant weighting W_f, W_b, A_t and the transfer function weighting $W_\Delta(s)$ in such a way that the three inequalities above ensure the control objectives described at the end of Section 2.

a. $\|T_{e_1 \to v_{node}}\|_\infty < \gamma < 1$

The vector of transfer functions $T_{e_1 \to v_{node}}$ is equal to $T_{f \to v_{node}} W_f$. As already mentioned, we will here choose W_f as a constant weighting. Consequently, the constraint $\|T_{e_1 \to v_{node}}\|_\infty < \gamma < 1$ in fact means:

$$\forall \omega, \quad \overline{\sigma}(T_{f \to v_{node}}(j\omega)) < \frac{\gamma}{|W_f|} < \frac{1}{|W_f|} \tag{25}$$

or equivalently:

$$\forall \omega, \quad \sqrt{T^*_{f \to v_{node}}(j\omega) T_{f \to v_{node}}(j\omega)} < \frac{\gamma}{|W_f|} < \frac{1}{|W_f|} \tag{26}$$

To justify this criterion, let us first consider the open-loop case i.e. the case where $K = 0$. The transfer vector $T_{f \to v_{node}}$ then reduces to $G_{f \to v_{node}}$. Due to the resonant nature of the considered system, the largest singular value $\overline{\sigma}(G_{f \to v_{node}})$ of the transfer vector between f and v_{node} will be made up of sharp peaks (as will be seen in e.g. Fig. 14). This will of course remain the case when a controller $K \neq 0$ will be applied to the system. However, since the controller K will be designed in such a way that Eq. (25) (and other constraints) holds with the smallest γ, the amplitude of these sharp peaks can be made smaller by a smart choice of the constant W_f (the larger W_f, the larger the peak reduction). Recall now the expression for the central energy, Eq. (10), given at the end of Section 4.1.2. Using this expression for the central energy and the sharp peak nature of the considered system, it is clear that a reduction of the peak amplitudes in $\overline{\sigma}(T_{f \to v_{node}})$ implies a reduction of the central energy.

It is to be noted that, due to the model reduction step of Section 4.3, $\overline{\sigma}(G_{f\rightarrow v_{node}})$ will only present peaks in the frequency band of interest $(\omega_{low}, \omega_{up})$ and will thus have low gain outside of this band. Consequently, by imposing Eq. (25), we will only reduce the peaks in the frequency band of interest. This is not a problem since the disturbance will only excite those specific peaks.

b. $\|T_{e_3\rightarrow z_u}\|_\infty < \gamma$

Even though the model reduction has been done with care (see Section 4.3), an H_∞ controller designed on the reduced-order model G could still destabilize the full-order model G^{full}. Ensuring that $\|T_{e_3\rightarrow z_u}\|_\infty < \gamma$ with $\gamma < 1$ will prevent this so-called spill-over problem to happen. Indeed, from Fig. 8, we see that $T_{e_3\rightarrow z_u}$ is equal to $W_\Delta T_{c\rightarrow u}$ where $T_{c\rightarrow u}$ is the complementary sensitivity function:

$$T_{c\rightarrow u} = (1 - KG_{V_a\rightarrow V_s})^{-1} KG_{V_a\rightarrow V_s} \tag{27}$$

To optimally choose the weighting function W_Δ, recall the robust stability result presented in Section 5.1.2. Using this result, if we choose W_Δ in such a way that the following holds:

$$\forall\omega,\ \overline{\sigma}(\Delta(j\omega)) \leqslant |W_\Delta(j\omega)| \tag{28}$$

where Δ is the relative error defined by Eq. (12), an H_∞ controller satisfying $\|T_{e_3\rightarrow z_u}\|_\infty = \|W_\Delta T_{c\rightarrow u}\|_\infty < 1$ will be guaranteed not only to stabilize G, but also G^{full}. To show this, let us first note that the part of the full-order model between V_a and V_s can be written for the Δ defined in Eq. (12) and satisfying Eq. (28) as

$$G^{full}_{V_a\rightarrow V_s} = G_{V_a\rightarrow V_s}(I + \Delta),$$

Let us also note that the closed-loop $G^{full}_{V_a\rightarrow V_s} \star K$ can be recast in a closed-loop (Δ, M_d) (see Fig. 7) with $M_d = T_{c\rightarrow u}$. Consequently, the desired stability property is a direct consequence of the robust stability result presented in Section 5.1.2. It is to be noted that, by virtue of this same robust stability result, the H_∞ controller will also stabilize all systems $\bar{G}$ that can be expressed as $\bar{G} = G_{V_a\rightarrow V_s}(I + \Delta)$ with a transfer matrix Δ satisfying Eq. (28).

Remark. The above approach will only lead to satisfactory results if the relative error Δ in Eq. (12) satisfies the following constraint:

$$\sup_{\omega\in(\omega_{low},\omega_{up})} \overline{\sigma}(\Delta(j\omega)) \leqslant 1. \tag{29}$$

Otherwise, the condition $\|W_\Delta T_{c\rightarrow u}\|_\infty < 1$ will imply that $\overline{\sigma}(T_{c\rightarrow u}(j\omega)) < 1$ in $(\omega_{low}, \omega_{up})$, which in turn implies that $G_{V_a\rightarrow V_s}K$ is small in $(\omega_{low}, \omega_{up})$. This contradicts the fact that $G_{V_a\rightarrow V_s}K$ should be large in $(\omega_{low}, \omega_{up})$ in order to have enough control effect. The expression Eq. (29) also gives a quality tag for the reduced-order model. As an example, the second step of the model reduction technique proposed in Section 4.3 is only necessary if Eq. (29) is not satisfied after the first step.

c. $\|T_{e_1\rightarrow z_u}\|_\infty < \gamma < 1$ and $\|T_{e_2\rightarrow z_u}\|_\infty < \gamma < 1$

These parts of the H_∞ criterion pertain to the limitation of the control effort. More precizely, they shape the transfer matrices between the external signals (the force f and the measurement noise vector b) and the vector of control inputs u. We have indeed that $T_{e_1\rightarrow z_u} = A_t W_\Delta T_{f\rightarrow u} W_f$ and $T_{e_2\rightarrow z_u} = A_t W_\Delta T_{b\rightarrow u} W_b$. Due to the scalar nature of the weightings, these parts of the criterion ensure:

$$\forall\omega,\ \overline{\sigma}(T_{f\rightarrow u}(j\omega)) < \frac{1}{|A_t W_\Delta(j\omega) W_f|} \tag{30}$$

$$\forall\omega,\ \overline{\sigma}(T_{b\rightarrow u}(j\omega)) < \frac{1}{|A_t W_b W_\Delta(j\omega)|} \tag{31}$$

As already mentioned, we will choose A_t and W_b as constant weightings. This simple choice is made possible by the shape of the frequency response of the transfer function weighting $W_\Delta(s)$ which will generally have high amplitude outside $(\omega_{low}, \omega_{up})$ since it must satisfy Eq. (28). Indeed, the presence of $|W_\Delta(j\omega)|$ in the above equations ensure that the (high frequency content) noise b will have little influence on the control input and that the control input will have a PSD which is mainly located in the frequency band of interest $(\omega_{low}, \omega_{up})$.

The constant weightings A_t and W_b can be used to limit the amplitude of the control effort (whose frequency content will be concentrated in $(\omega_{low}, \omega_{up})$ via $|W_\Delta(j\omega)|$) and we can make a distinction between the contribution of f and b in this control effort by independently tuning A_t and W_b. A good practice is to increase these constants as long as the H_∞ criterion remains solvable for a constant $\gamma < 1$. As already mentioned, the required control efforts (and thus the extent with which the constants can be increased) depends on the desired central energy reduction (see item a. above).

5.3. Controller reduction and discretization

As mentioned in Section 3, for the ease of the implementation, the obtained H_∞ controller will be reduced without degrading the performance. Due to the choice of the weighting functions discussed in the previous subsection, the obtained H_∞ controller will have low gain dynamics outside the frequency range of interest. Moreover, these dynamics outside the frequency range of interest are not/less important for the control objectives and can therefore be removed in the reduced-order controller. Consequently, the simple and widely used Balanced Truncation method [41] can be applied to perform controller reduction. More precisely, we determine the controller with the lowest order that nevertheless preserve the stability and the level of performance with the full-order model.

Since the controller will be implemented in a digital signal processor[12], the obtained reduced-order controller has finally to be discretized. The sampling time should be chosen small enough to guarantee that the frequency response of the discrete-time controller remains close to the continuous-time controller at frequencies lower than ω_{up}.

6. Application

6.1. Beam-piezo system model

Following the procedure in Section 4.1, we derive a state-space model $G^{full}(\theta_{init})$ (see Eq. (4)-(5)) using COMSOL. Since the frequency range of interest is $(600, 3000)\ rad/s$, the dimension of the vector $\eta(t)$ in Eq. (4) is chosen equal to 20. The frequency ω_{20} corresponding to the 20^{th} mode is indeed slightly larger than $\omega_{up} = 3000\ rad/s$. The dimension N_z of the vector ν_{node} is here chosen equal to 19. Recall also that V_a and V_s will pertain to 10^{th} and 16^{th} PZT pairs and the 5^{th} and 11^{th} PZT pairs, respectively. Consequently, the state vector x in the derived state-space model $G^{full}(\theta_{init})$ is of dimension 42.

Let us now compare the frequency response of $G^{full}(\theta_{init})$ and the one of the experimental setup. A very accurate non-parametric estimate of the latter can be derived using a frequency analyzer (an HP 35652B in our case). Such a frequency analyzer deduces an estimate of the frequency response of a SISO transfer function by averaging out the ratio of the Fourier transforms of the output and the input over multiple experiments. In Fig. 9 (where we focus on the dynamics between V_a and V_s), we observe a large discrepancy between this accurate estimate of the frequency response of the setup (in blue) and the frequency response of the initial model $G^{full}(\theta_{init})$ (in yellow). Such a discrepancy is also visible for the other dynamics of the system. To obtain a more accurate parametric model of the setup, we have applied the grey-box identification procedure of Section 4.2 yielding the model $G^{full}(\theta_{id})$. Note that, in this identification procedure, all input-output data sets have been first pre-filtered by a band pass filter focusing on the frequency range of interest. As shown in Fig. 10 for the dynamics between V_a and V_s, the obtained identified model $G^{full}(\theta_{id})$ has a frequency response which is much closer to the accurate non-parametric estimate obtained via the frequency analyzer. The model $G^{full}(\theta_{id})$ will therefore be used in the sequel for controller design (after a reduction step).

The model reduction approach proposed in Section 4.3 is applied to $G^{full}(\theta_{id})$. By removing the poles outside the frequency band of interest $(600, 3000)\ rad/s$, the MFT step (the first step) yields a model of order 24. As shown in blue in Fig. 11, the maximum singular value $\overline{\sigma}(\Delta(j\omega))$ of the modeling error $\Delta(j\omega)$ (see Eq. (12)) in the frequency band of interest is excessive: Eq. (29) is far from satisfied. The second step is therefore performed and it yields the reduced-order model whose difference $\Delta(j\omega)$ with the full-order model now satisfies Eq. (29), as can be seen in Fig. 11. When looking at the dynamics between V_a and V_s in the frequency range of interest, we observe in Fig. 12 that, with respect to the model obtained after the first model reduction step, the frequency response of the reduced-order model obtained after the second step is closer to the one of the full-order model, especially at the anti-resonances. The model (15) (denoted G) will therefore be the one that will be used for control design (its order is also equal to 24).

[12] DSpace (Type: DS1104) in our case

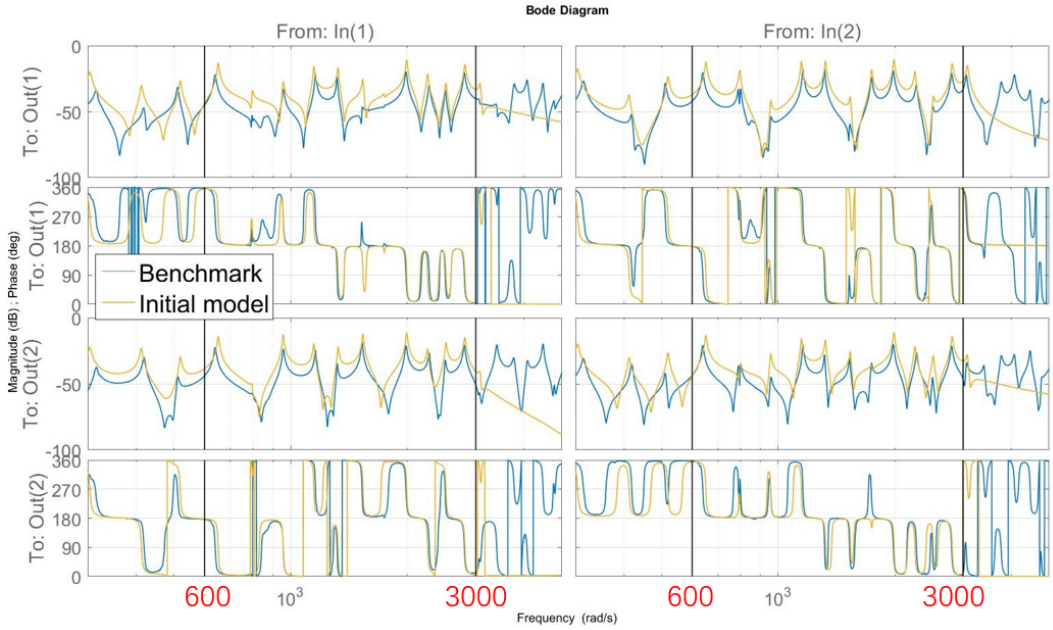

Fig. 9. Comparison of the frequency response from V_a to V_s: non-parametric estimate obtained with the frequency analyzer (blue) and initial model $G^{full}_{V_a \to V_s}(\theta_{init})$ (yellow)

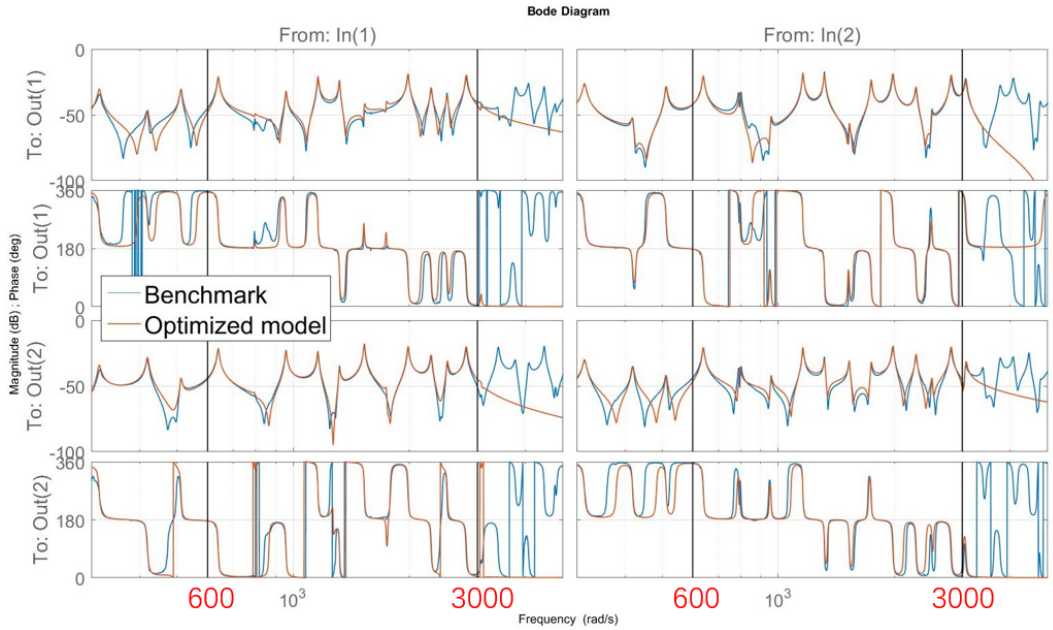

Fig. 10. Comparison of the frequency response from V_a to V_s: non-parametric estimate obtained with the frequency analyzer (blue) and identified model $G^{full}_{V_a \to V_s}(\theta_{id})$ (red)

6.2. H_∞ controller design for the beam-piezo system

The controller will be designed using the procedure described in Section 5.2. Let us first discuss the choice of the weighting $W_\Delta(s)$. This weighting is chosen as a simple transfer function that satisfies Eq. (28). The modulus of the frequency response of the chosen W_Δ is represented in Fig. 13 and we observe that Eq. (28) is indeed satisfied. To

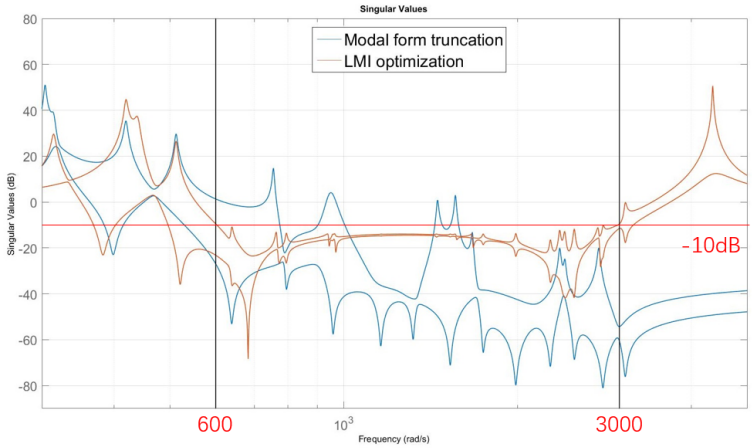

Fig. 11. $\overline{\sigma}(\Delta(j\omega))$ after the first model reduction step (blue) and after the second model reduction step (red)

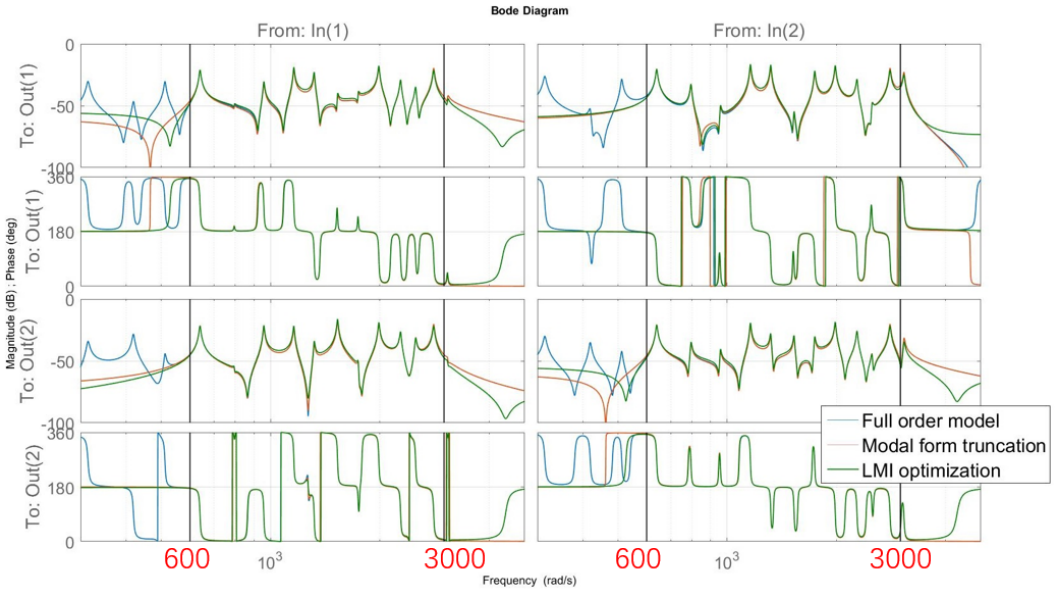

Fig. 12. Frequency response of $G^{full}_{V_a \to V_s}$ (blue), of $G_{V_a \to V_s}$ after the first model reduction step (red) and of this model after the second model reduction step

choose the constant weighting W_f, let us first consider the quantity $\overline{\sigma}(G_{f \to v_{node}}(j\omega))$ (represented in blue in Fig. 14.a). We observe peaks up to $-10\ dB$ in this figure. In order to reduce the vibration energy, we will need to reduce these peaks. After some trial and error, we have here decided to impose that, in closed-loop, $\overline{\sigma}(T_{f \to v_{node}}(j\omega))$ will not present peaks that are larger than $-19\ dB$ and we therefore choose $W_f = 6.9$. Given this choice of W_f, we then reduce the constant weightings A_t and W_b as much as possible to keep the H_∞ criterion solvable with a $\gamma < 1$. This is done in order to reduce as much as possible the control efforts while guaranteeing $\forall\omega$, $\overline{\sigma}(T_{f \to v_{node}}(j\omega)) < -19\ dB$. The values that are finally chosen are $A_t = 3.9$ and $W_b = 1$ which, together with the other weightings[13], lead to a controller K of order 52 for which the H_∞ criterion holds with $\gamma = 0.9923$. The frequency response of this controller K is given in blue in Fig. 15.

The closed-loop quantity $\overline{\sigma}(T_{f \to v_{node}}(j\omega))$ obtained with this controller is compared with the open-loop quan-

[13] The gain of the power amplifier (see Fig. 8) is here given by $A_p = -10$ and the Pade filter F_d approximates a delay of of $1.6 \times 10^{-4}\ s$.

tity $\overline{\sigma}(G_{f\to v_{node}}(j\omega))$ in Fig. 14.a and we observe that most of the peaks are severely reduced (and that, as imposed, $\forall\omega,\ \overline{\sigma}(T_{f\to v_{node}}(j\omega)) < -19\ dB$). As will be seen later, this peak reduction is performed with an acceptable control action for typical disturbance force f. Further reduction would of course be possible, but at the cost of higher control actions (and thus more energy consumption).

As imposed in the H_∞ criterion, the controller K designed with the reduced-order model G indeed stabilizes the full-order model $G^{full}(\theta_{id})$ and, when this controller is applied to $G^{full}(\theta_{id})$, we obtain a very similar peak reduction as with the reduced-order model G (compare Fig. 14.a and Fig. 14.b). Note that, as expected, only the modes in $(600, 3000)\ rad/s$ are reduced in the closed-loop made up of K and $G^{full}(\theta_{id})$ (see Fig. 14.b).

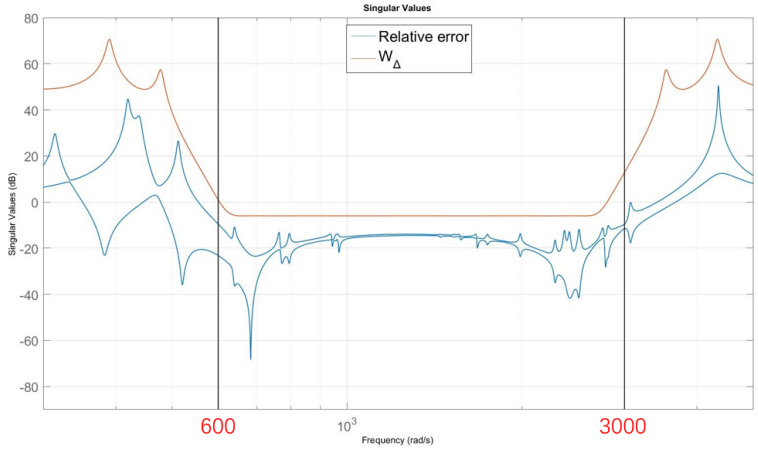

Fig. 13. $\overline{\sigma}(\Delta(j\omega))$ (blue) and $|W_\Delta(j\omega)|$ (red)

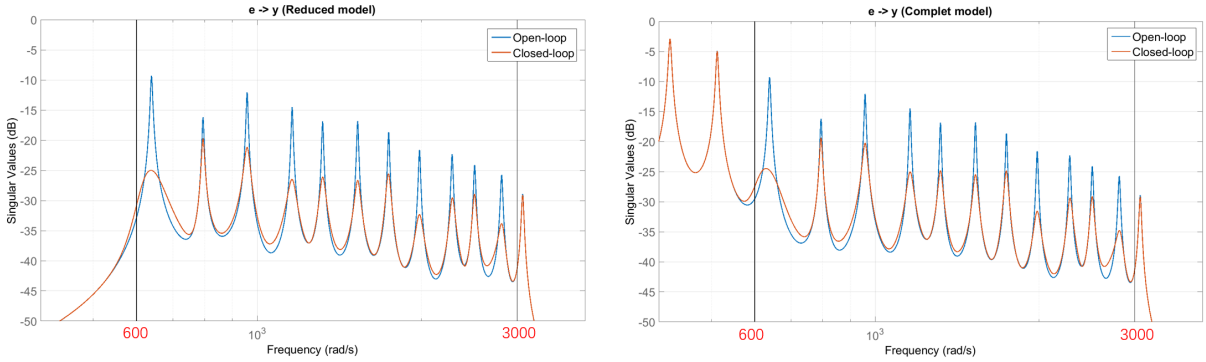

Fig. 14. On the left (Figure a), $\overline{\sigma}(G_{f\to v_{node}}(j\omega))$ (blue) and $\overline{\sigma}(T_{f\to v_{node}}(j\omega))$ (red) when the controller K is applied to the reduced-order model G. On the right (Figure b), $\overline{\sigma}(G^{full}_{f\to v_{node}}(j\omega))$ (blue) and $\overline{\sigma}(T_{f\to v_{node}}(j\omega))$ (red) when the controller K is applied to the full-order model G^{full}

6.3. Reduced-order controller

Using Balanced Truncation, the order of the controller K can be reduced to 30 without destabilizing the full-order model and without significant change in the closed-loop performance of the controller. Fig. 16 indeed shows the almost perfect match between the closed-loop quantities $\overline{\sigma}(T_{f\to v_{node}}(j\omega))$ obtained when applying the full-order controller K (red) and the reduced-order controller K_{red} (yellow) to the full-order model. We have also performed simulations with both controllers and found that the level of the control efforts remains very similar even in the presence of measurement noise. It is to be noted that we do not evaluate the performance of the reduced-order

controller based on the chosen H_∞ criterion since this criterion is only a mathematical formulation of the desired performance level and since there are controllers that do not (perfectly) satisfy the H_∞ criterion, but that nevertheless lead to a satisfactory performance level in terms of the stabilization of the full-order model, the vibration attenuation and the level of the control efforts. The frequency response of the reduced-order controller K_{red} is represented in red in Fig. 15 and compared with the one of the full-order controller K. It is to be noted that both K and K_{red} are stable transfer functions.

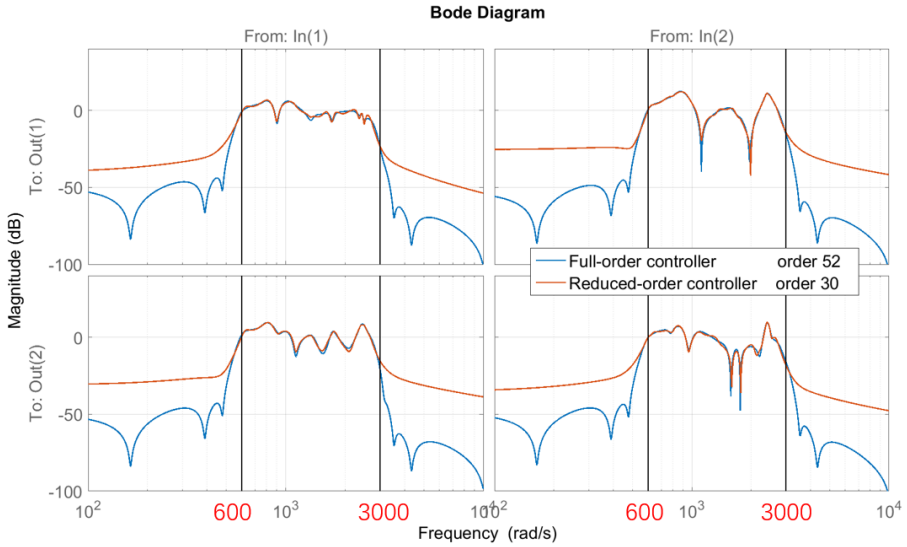

Fig. 15. Modulus of the frequency response of the full-order controller K (blue) and of the reduced-order controller K_{red} (red)

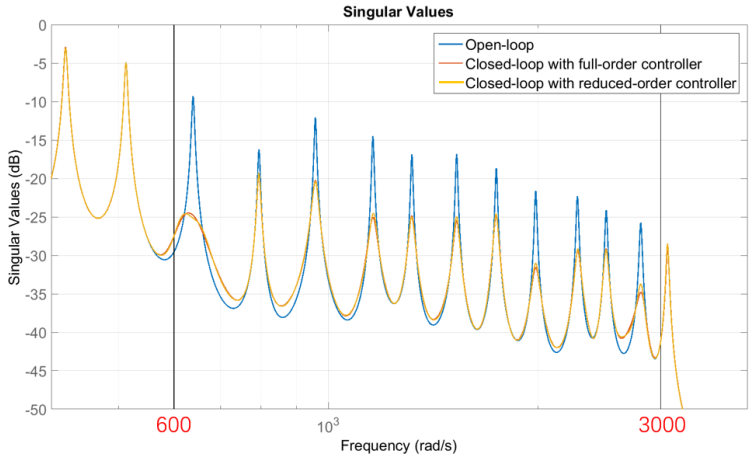

Fig. 16. $\overline{\sigma}(G^{full}_{f\to v_{node}}(j\omega))$ (blue), $\overline{\sigma}(T_{f\to v_{node}}(j\omega))$ when the full-order controller is applied to the full-order model (red) and $\overline{\sigma}(T_{f\to v_{node}}(j\omega))$ when the reduced-order controller is applied to the full-order model (yellow)

6.4. Proportional central energy reduction

Let us analyze further the performance of the closed-loop made up of the reduced-order controller K_{red} and the full-order model G^{full}. By comparing the blue and yellow curves in Fig. 16, we can expect that the reduction of the vibration energy in the central zone will be important. Using Eq. (10), the reduction rate of the proportional central energy $\overline{E^p_{cent}}$ can be deduced as follows:

$$r_e^p = \left(1 - \frac{\left(\overline{E_{cent}^p}\right)_{CL}}{\left(\overline{E_{cent}^p}\right)_{OL}}\right) \times 100\% = \left(1 - \frac{\|T_{f\to v_{node}} L_f\|_2^2}{\|G^{full}_{f\to v_{node}} L_f\|_2^2}\right) \times 100\% \tag{32}$$

where $T_{f\to v_{node}}$ is here the closed-loop transfer vector between f and v_{node} in the loop made up of K_{red} and G^{full} and where $L_f(s)$ is a transfer function such that the PSD of f is given by $|L_f(j\omega)|^2$. When L_f is given by a band-pass filter in the frequency range of interest $(600,\ 3000)\ rad/s$, the reduction rate r_e^p is equal to 59.6 %. When L_f corresponds to the PSD of the actual disturbance force f generated by the shaker, the reduction rate r_e^p is then equal to 62.5 %.

The above expression neglects the effect of the measurement noise b on v_{node} in the closed-loop situation. We have therefore performed simulations by adding a realistic measurement noise and have observed that the effect of the measurement noise b on v_{node} is negligible. These simulations have also allowed us to verify that the control efforts (due to the presence of both f and b) remain at all time in the working range of the actuators.

Let us now verify whether this control performance (in particular the large reduction rate) can also be achieved in practice when the reduced-order controller K_{red} is applied on the real setup.

6.5. Experimental results

To evaluate the actual reduction rate obtained on the experimental setup, we will compare the open-loop situation where the force f (of PSD $|L_f(j\omega)|^2$) is applied to the beam without control actions ($V_a = 0$) and the closed-loop situation where the force f is applied and the controller K_{red} is active (the controller is implemented in a DSpace environment (DS1104 in our case)).

In both situations, $v_{node_i}(t) = v(x_i, t)$ is measured via the laser velocimeter at the $N_z = 19$ nodes x_i that have been chosen in the central zone[14]. In the top part of Fig. 17, we represent, as a function of the time, the vibration velocity $v_{node_i}(t) = v(x_i, t)$ of one of these nodes during an experiment where the controller is kept inactive (open-loop situation) from $t = 0$ till $t = 10$ seconds and then the controller is activated for 10 seconds, etc... We can clearly observe the velocity reduction when the controller is active. Evaluating the (proportional) vibration energy $\overline{E_{node_i}^p}$ at node i as the average value of $v_{node_i}^2(t)$ in the open-loop and closed-loop situation, the reduction of the vibration energy at this particular node is equal to 65.4%. This reduction rate is consistent with the one observed in simulations (with and without measurement noise) and which were respectively equal to 63.1% and 65.1%.

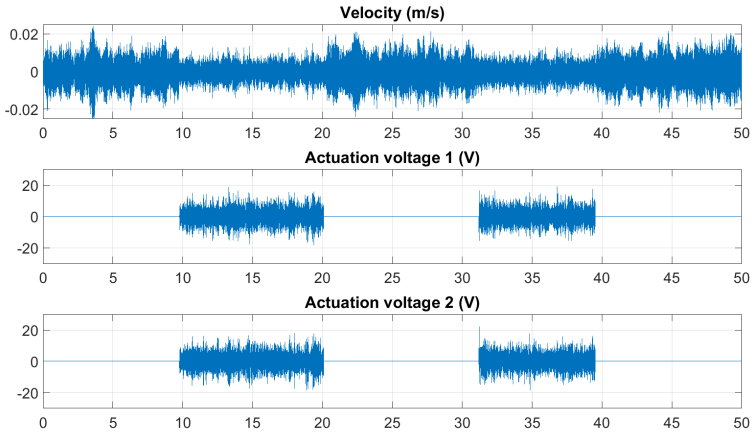

Fig. 17. Velocity of an arbitrary point in the central zone (top figure) for an experiment consisting of switching on and off the controller K_{red} every 10 seconds, first element of V_a (mid-figure) and second element of V_a (bottom figure)

In Fig. 17, the voltages applied on the two actuators (i.e. V_a) are also represented and they remain at all time within the working limits of the piezo-actuators.

[14] in fact, 19 different experiments have to be performed to obtain this result since only one laser velocimeter is available

Let us now formally evaluate the reduction rate of the energy in the central zone obtained on the experimental setup using the measurements $\nu_{node_i}(t) = \nu(x_i, t)$ at all 19 nodes. For this purpose, we will estimate the central energy $\overline{E^p_{cent}}$ in the open-loop and the closed-loop situations as $\overline{E^p_{cent}} = \sum_{i=1}^{19} \overline{E^p_{node_i}}$ (see Eq. (9)).

Based on the central energy obtained in this way in open and in closed loop[15], we have evaluated the energy reduction rate to 58.9%. We thus observe that this estimate of the experimental reduction rate is very close to the one that is theoretically computed on the loop made up of the controller K_{red} and of the full-order model $G^{full}(\theta_{id})$ (i.e. 62.5%).

It can therefore be concluded that the model deduced from grey-box identification $G^{full}(\theta_{id})$ was a good model of the experimental setup for control purpose. It is also to be stressed that the model improvement via grey-box identification is necessary. Indeed, if the H_∞ controller is designed based on the initial model $G^{full}(\theta_{init})$ and then applied on $G^{full}(\theta_{id})$, the obtained energy reduction rate would go down to only 46%.

Let us further illustrate the energy reduction rate of 58.9%. Using the measurements $\nu_{node_i}(t) = \nu(x_i, t)$ obtained at all 19 nodes and the applied disturbance force f, we use the frequency analyzer to estimate the frequency responses of the transfer functions between f and ν_{node_i} ($i = 1...19$) in the open-loop and the closed-loop situations. We subsequently compute, for both the open-loop and the closed-loop situations, the largest singular value of the vector made up of these 19 frequency responses. These two singular values are plotted as a function of the frequency in Fig. 18. Even though we can see some discrepancies between this figure and Fig. 16 (that can be due among other things to the inherent difficulties in this validation step of pointing the laser velocimeter at exactly the same 19 positions as during the identification procedure), we also clearly observe that the eleven modes in the frequency band of interest $(600, 3000)$ rad/s are effectively controlled and most of them have more than 10 dB reduction with 15 dB being the maximum reduction. Such peak reductions can also be observed in other papers (see e.g. [42, 10, 11, 12, 14]), but on fewer resonance peaks (meaning that the reduction rate will be smaller). Note moreover that the control problem is here more complex since the energy reduction is achieved in a zone where there are no actuators and no sensors.

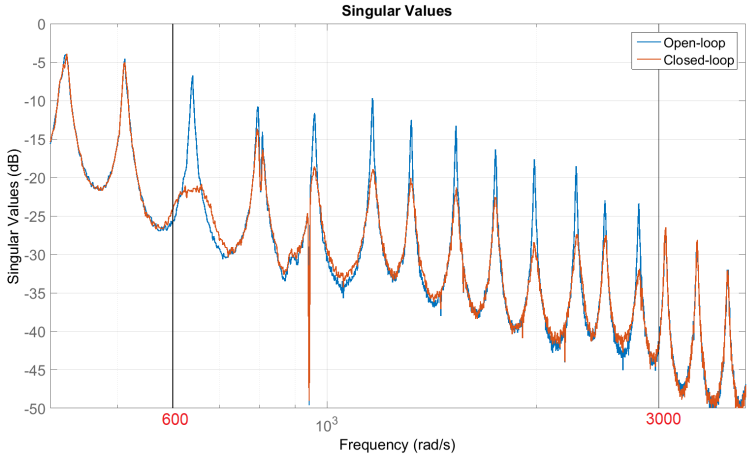

Fig. 18. $\overline{\sigma}(G_{f\to\nu_{node},m}(j\omega))$ (blue) and $\overline{\sigma}(T_{f\to\nu_{node},m}(j\omega))$ (red) measured on the experimental set-up

Our objective was thus to reduce the vibration in the central zone of the beam. One could wonder what happens in the other parts of the beam. We have therefore also measured the velocity at one point on the left side of the central zone and at one point on the right side of this central zone (see Fig. 19) and we have observed that the vibration at these two points is also reduced in closed-loop: the reduction of the vibration energy at these two nodes are respectively equal to 56.8% and 49.8%, however smaller than that of the measured point in the central zone (i.e. 65.4%).

[15] It is to be noted that, as opposed to what is done for $\left(\overline{E^p_{cent}}\right)_{CL}$ in Eq. (32), the above manner to evaluate the central energy in the closed-loop situation considers the influence of both the disturbance force f and the measurement noise b.

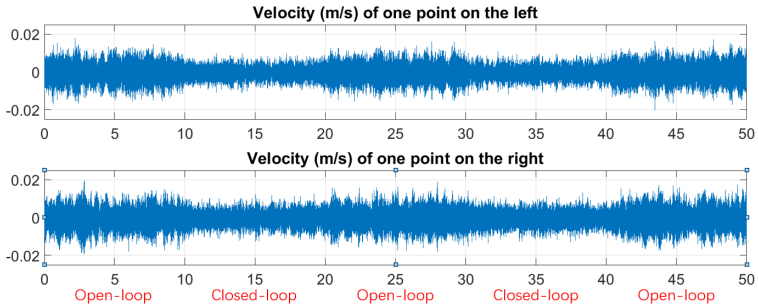

Fig. 19. Velocity of one point on the left (top figure), velocity of one point on the right (bottom figure)

7. Conclusion

This paper proposes a methodology to solve a particular vibration control problem, that is to reduce the vibration in a specific zone of a flexible smart structure where neither actuation nor sensing is possible. This methodology is applied on a long thin aluminium beam with PZT where the vibration in the central zone is to be reduced. A combination of physical and data-based modeling allows us to obtain an accurate model and then a multi-variable H_∞ controller is computed. The simulation and the experimental results prove that the obtained model is very close to the actual experimental set-up and the controller is able to effectively reduce the vibration in the central zone of the beam under a force disturbance over a large frequency range. A very high reduction rate is obtained. It should be noted that the obtained controller is centralized, i.e. it processes all sensor data to generate all feedback control signals. The drawback of this approach is the complexity of the physical connections and the high computational burden on the centralized processor. The future work will focus on decentralized or distributed control with numerous localized controllers working together, reducing in this way the physical connection complexity and the computational burden.

Appendix A. PZT selection

If a mode must be controlled, it should effectively be excited/detected by the actuator/sensor. This means that the peaks corresponding to all these modes must be clearly seen in the frequency response with a relatively high magnitude. Therefore, the frequency response, which can be measured by a frequency analyzer, between different actuators and sensors are compared and we found that the frequency response from one actuator to one sensor always has some peaks that can not be clearly seen or only have low magnitude. Such peaks are not always at the same frequencies in the response between other actuator and sensor. Fig. A.20 shows an example of this phenomenon. The blue line and red line are respectively the frequency response from the 10^{th} to the 11^{th} PZT pair and from the 16^{th} to the 11^{th} PZT pair. At the frequency circled by ellipse 1, the red line shows a much higher peak than the blue line while at the frequencies circled by ellipse 2 and 3, an opposite situation occurs. This phenomenon can be explained by the position of the PZT pair. If a PZT pair is located close to the node of a certain mode shape, this mode cannot be effectively excited or detected because the deformation at the node is very weak. Therefore, the corresponding peak in the frequency response will be very small or even disappear (it in fact depends on how close to the node the PZT pair is). This also proves that a SISO controller is not enough to control all the modes. As a result, the PZT pairs used for control are chosen in the way that when all the frequency responses between the chosen actuators and sensors are represented together in the same plot, all the peaks corresponding to the to-be-controlled modes can be clearly seen with a relatively high magnitude. At the same time, in order to balance the control effect, there should be at least one actuator and one sensor on each side of the central zone.

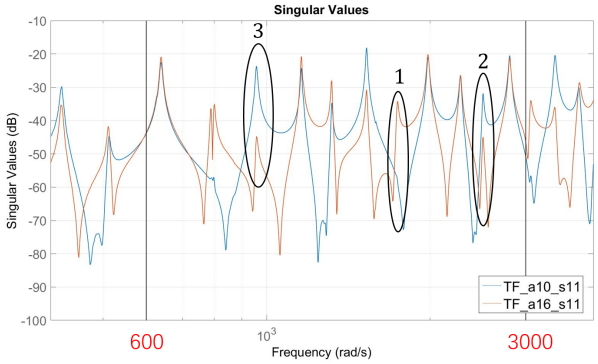

Fig. A.20. Frequency response from the 10^{th} to the 11^{th} PZT pair (blue) and from the 16^{th} to the 11^{th} PZT pair (red)

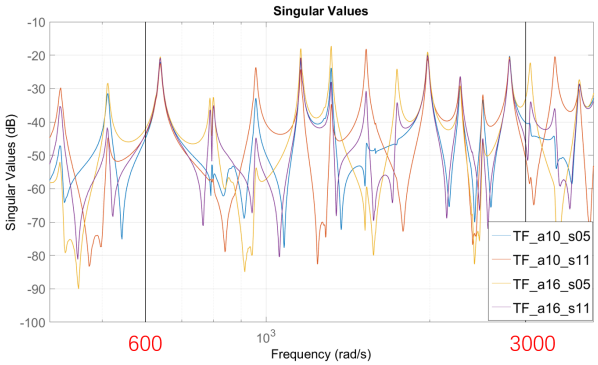

Fig. A.21. Frequency response comparison: the 10^{th}, the 16^{th} to the 5^{th}, the 11^{th}

Finally, in order to avoid local strain, the chosen actuators and sensors should not be too close to each other. Indeed, according to [43], when a piezoelectric patch is used as actuator, in addition to excite vibration modes, it

also induces a local deformation. If the sensor is too close to the actuator, this local deformation can perturb the measurement of the vibration movement.

Considering all the above considerations and comparing different frequency responses, the 10^{th} and the 16^{th} PZT pairs are finally chosen as actuators and the 5^{th} and the 11^{th} PZT pairs as sensors (see Fig. 4). Indeed, as can be seen in Fig. A.21, all the peaks of interest are clearly seen. Moreover, the chosen actuators and sensors are not too close to each other and we have an actuator and a sensor on both sides of the central zone.

Remark. Even though more systematic approaches for the selection of the PZT pairs are available in the literature (see e.g. [44]), the simple approach above was satisfactory for our purpose.

Appendix B. Governing equation and damping effect

The normalized governing equation with the first N modes and N_P PZT pairs (both actuators and sensors) is in the form below:

$$\begin{bmatrix} M_{mode} & 0 \\ 0 & 0 \end{bmatrix} \begin{bmatrix} \ddot{\eta}(t) \\ \ddot{V}(t) \end{bmatrix} + \begin{bmatrix} K_{mode} & E \\ -E^T & R \end{bmatrix} \begin{bmatrix} \eta(t) \\ V(t) \end{bmatrix} = \begin{bmatrix} F \cdot f(t) \\ Q(t) \end{bmatrix} \tag{B.1}$$

where $R = diag(r_1, r_2, \cdots, r_{N_P})$ is the capacity matrix with r_j the capacity of the j^{th} PZT pairs and E the electromechanical coupling matrix. $V(t)$ and $Q(t)$ are respectively the voltage vector and the charge vector of all the PZT pairs. Other parameters and variables have the same meaning as described in Section 4.1.

Remark. In COMSOL, the first N modes are solved under the condition that there is no voltage excitation on PZT, which means $V(t) = 0$. In fact, Eq. (B.1) is considered as a truncated model of the actual system because the actual system contains an infinite number of modes. In order to correct the error introduced by the truncation, stationary analysis is also done where the capacity matrix R is corrected to make sure that when PZT is excited by a constant voltage (for example $V(t) = 1$), the induced charge $Q(t)$ of Eq. (B.1) and of the actual system with infinite modes are equal.

Now the actuators and sensors are considered separately. Denote V_a the actuator voltage vector and V_s the sensor voltage vector. The voltages of the unused PZT pairs are set to zero. Then, Eq. (2) can be obtained and also the so called modal equation:

$$M_{mode} \cdot \ddot{\eta}(t) + K_{mode} \cdot \eta(t) + E_a \cdot V_a(t) + E_s \cdot V_s(t) = F \cdot f(t) \tag{B.2}$$

where E_a, E_s, R_s, $V_a(t)$, $V_s(t)$ and $Q_s(t)$ are exactly the same parameters and variables mentioned in Section 4.1 and they are respectively part of E, R, $V(t)$ and $Q(t)$.

Eq. (B.2) does not have damping effect. The damping effect corresponds to the first derivative term. Denote $\mathcal{X}$ the coefficient of the first derivative term, then the modal equation with damping effect is as below:

$$M_{mode} \cdot \ddot{\eta}(t) + \mathcal{X} \cdot \dot{\eta}(t) + K_{mode} \cdot \eta(t) + E_a \cdot V_a(t) + E_s \cdot V_s(t) = F \cdot f(t). \tag{B.3}$$

Here, the Rayleigh Damping [45] is introduced which defines $\mathcal{X}$ as:

$$\mathcal{X} = \kappa_a M_{mode} + \kappa_s K_{mode}, \tag{B.4}$$

where κ_a and κ_s are two damping constants. Eq. (1) is thus obtained.

Appendix C. Relative error minimization by LMI

Denote G a full-order model whose state-space representation is (A, B, C, D) and G_r the truncated model to be optimized whose state-space representation is (A_r, B_r, C_r, D_r). G and G_r are close in $(\underline{\omega}, \overline{\omega})$ where G_r keeps the poles of G which means:

$$\lambda(A_r) \subset \lambda(A)$$

where $\lambda(\cdot)$ denotes the set of eigenvalues. Eq. (14) is rewritten as:

$$\begin{aligned} &\min_{C_r,D_r} \ \gamma \\ &\quad \textit{such that} \\ &\quad \forall\omega \in (\underline{\omega},\overline{\omega}),\ \overline{\sigma}\left(G_r(j\omega)^{-1}(G(j\omega)-G_r(j\omega))\right) < \gamma \end{aligned} \tag{C.1}$$

In order to solve the above problem, necessary approximating has to be made because the constraint in Eq. (C.1) can not be transformed into LMI constraints. That is the reason way the following proposition is made.

Proposition 1. $\forall\omega$ such that $\overline{\sigma}\left(G(j\omega)^{-1}(G(j\omega)-G_r(j\omega))\right) \ll 1$ then:

$$\overline{\sigma}\left(G(j\omega)^{-1}(G(j\omega)-G_r(j\omega))\right) \approx \overline{\sigma}\left(G_r(j\omega)^{-1}(G(j\omega)-G_r(j\omega))\right) \ll 1 \tag{C.2}$$

Proof.

$$\begin{aligned} &\overline{\sigma}\left(G(j\omega)^{-1}(G(j\omega)-G_r(j\omega))\right) = \overline{\sigma}\left(I - G(j\omega)^{-1}G_r(j\omega)\right) \ll 1 \\ \Leftrightarrow\ & G(j\omega)^{-1}G_r(j\omega) \approx I \\ \Leftrightarrow\ & \overline{\sigma}\left(G_r(j\omega)^{-1}G(j\omega)\right) = \frac{1}{\underline{\sigma}\left(G(j\omega)^{-1}G_r(j\omega)\right)} \approx 1 \end{aligned}$$

where I is identity. Then,

$$\begin{aligned} \overline{\sigma}\left(G_r(j\omega)^{-1}(G(j\omega)-G_r(j\omega))\right) &= \overline{\sigma}\left(G_r^{-1}(j\omega)G(j\omega)G(j\omega)^{-1}(G(j\omega)-G_r(j\omega))\right) \\ &\leqslant \overline{\sigma}\left(G_r^{-1}(j\omega)G(j\omega)\right)\overline{\sigma}\left(G(j\omega)^{-1}(G(j\omega)-G_r(j\omega))\right) \\ &\ll 1 \end{aligned}$$

□

Using Proposition 1, Eq. (C.1) is approximated by:

$$\begin{aligned} &\min_{C_r,D_r} \ \gamma \\ &\quad \textit{such that} \\ &\quad \forall\omega \in (\underline{\omega},\overline{\omega}),\ \overline{\sigma}\left(G(j\omega)^{-1}(G(j\omega)-G_r(j\omega))\right) < \gamma \end{aligned} \tag{C.3}$$

The solution of Eq. (C.1) is approximately the solution of Eq. (C.3) which can be directly transformed into LMI constrains as described in the following theorem:

Theorem 2. *Consider G, the model of an LTI continuous system with the state-space representation denoted as (A, B, C, D), and G_r, a reduced model of G with the state-space representation denoted as (A_r, B_r, C_r, D_r) such that $\lambda(A_r) \subset \lambda(A)$. γ is a real positive number. The solution of Eq. (C.3) is given by solving the following LMI problem:*

$$\begin{aligned} &\min_{C_r,D_r,P\in\mathbb{C}^{n_a\times n_a}} \ \gamma^2 \\ &\quad \textit{such that} \\ &\quad P + P^* < 0,\ K + K^* > 0 \end{aligned} \tag{C.4}$$

where

$$K = XN + Q \tag{C.5}$$

$$X = \left[\begin{array}{c|ccc} P & \multicolumn{3}{c}{0} \\ \hline 0 & C_r & D_r & 0 \\ & 0 & 0 & \gamma^2 I \end{array}\right],\quad N = \left[\begin{array}{cc|cc} \multicolumn{2}{c|}{\widetilde{A}} & \multicolumn{2}{c}{\widetilde{B}} \\ \hline 0 & -E_{r\delta} & 0 & F_{r\delta} \\ 0 & 0 & 0 & -I \\ 0 & 0 & 0 & \frac{I}{2} \end{array}\right],\quad Q = \left[\begin{array}{cc|cc} B_\delta B_\delta^*/2 & 0 & 0 & 0 \\ 0 & 0 & 0 & 0 \\ \hline D_\delta B_\delta^* & 0 & D_\delta D_\delta^*/2 & D_\delta \\ B_\delta^* & 0 & 0 & 0 \end{array}\right]$$

$$\widetilde{A} = \begin{bmatrix} A_\delta^* & 0 \\ 0 & A_{r\delta} \end{bmatrix},\ \widetilde{B} = \begin{bmatrix} C_\delta^* & 0 \\ 0 & B_{r\delta} \end{bmatrix},\ E_{r\delta} = (I + \frac{j}{\underline{\omega}} A_r)^{-1},\ F_{r\delta} = \frac{j}{\underline{\omega}} E_{r\delta} B_r$$

$$\begin{aligned}
A_\delta &= -\overline{\omega} I - j(1 - \frac{\overline{\omega}}{\underline{\omega}}) A (I + \frac{j}{\underline{\omega}} A)^{-1}, & B_\delta &= -j(1 - \frac{\overline{\omega}}{\underline{\omega}})(I + \frac{j}{\underline{\omega}} A)^{-1} B, \\
C_\delta &= C(I + \frac{j}{\underline{\omega}} A)^{-1}, & D_\delta &= D - \frac{j}{\underline{\omega}} C (I + \frac{j}{\underline{\omega}} A)^{-1} B, \\
A_{r\delta} &= -\overline{\omega} I - j(1 - \frac{\overline{\omega}}{\underline{\omega}}) A_r (I + \frac{j}{\underline{\omega}} A_r)^{-1}, & B_{r\delta} &= -j(1 - \frac{\overline{\omega}}{\underline{\omega}})(I + \frac{j}{\underline{\omega}} A_r)^{-1} B_r, \\
C_{r\delta} &= C_r (I + \frac{j}{\underline{\omega}} A_r)^{-1}, & D_{r\delta} &= D_r - \frac{j}{\underline{\omega}} C_r (I + \frac{j}{\underline{\omega}} A_r)^{-1} B_r.
\end{aligned} \tag{C.6}$$

and n_a the dimension of $\widetilde{A}$.

Problem (C.4) is a linear cost minimization problem. There exist efficient algorithms to solve this problem, see [38]. The proof of **Theorem 2** can be found in [31].

References

[1] A. Preumont, Vibration Control of Active Structures, An Introduction, 3rd Edition, Springer, Dordrecht, 2011. doi:10.1007/978-94-007-2033-6.

[2] T. Oomen, E. Grassens, F. Hendriks, Inferential motion control: Identification and robust control framework for positioning an unmeasurable point of interest, IEEE Transactions on control systems technology 23 (4) (2015) 1602–1610.

[3] S. Khot, N. Yelve, R. Tomar, S. Desai, S. Vittal, Active vibration control of cantilever beam by using PID based output feedback controller, Journal of Vibration and Control 18 (3) (2012) 366–372. doi:10.1177/1077546311406307.

[4] V. Gupta, M. Sharma, N. Thakur, Active structural vibration control: Robust to temperature variations, Mechanical Systems and Signal Processing 33 (2012) 167–180. doi:10.1016/j.ymssp.2012.07.009.

[5] S. Y. Wang, S. T. Quek, K. K. Ang, Vibration control of smart piezoelectric composite plates, Smart Materials and Structures 10 (4) (2001) 637. doi:10.1088/0964-1726/10/4/306.

[6] Z. Qiu, X. Zhang, H. Wu, H. Zhang, Optimal placement and active vibration control for piezoelectric smart flexible cantilever plate, Journal of Sound and Vibration 301 (3) (2007) 521–543. doi:10.1016/j.jsv.2006.10.018.

[7] T. Hegewald, D. J. Inman, Vibration suppression via smart structures across a temperature range, Journal of Intelligent Material Systems and Structures 12 (3) (2001) 191–203. doi:10.1106/YX1U-GOGO-HWOU-7DH8.

[8] F. Palacios-Quiñonero, J. Rubió-Massegú, J. M. Rossell, H. R. Karimi, Vibration control for adjacent structures using local state information, Mechatronics 24 (4) (2014) 336–344.

[9] F. Palacios-Quiñonero, J. Rubió-Massegú, J. Rossell, H. Karimi, An effective computational design strategy for H_∞ vibration control of large structures with information constraints, Engineering Structures 171 (2018) 298–308.

[10] A. Koszewnik, The optimal vibration control of the plate structure by using piezo-actuators, in: Carpathian Control Conference (ICCC), 2016 17th International, IEEE, 2016, pp. 358–363. doi:10.1109/CarpathianCC.2016.7501123.

[11] A. Loghmani, M. Danesh, M. K. Kwak, M. Keshmiri, Vibration suppression of a piezo-equipped cylindrical shell in a broad-band frequency domain, Journal of Sound and Vibration 411 (2017) 260–277. doi:10.1016/j.jsv.2017.08.051.

[12] I. R. Petersen, H. R. Pota, Minimax LQG optimal control of a flexible beam, Control Engineering Practice 11 (11) (2003) 1273–1287. doi:10.1016/S0967-0661(02)00240-X.

[13] J. Maruani, I. Bruant, F. Pablo, L. Gallimard, A numerical efficiency study on the active vibration control for a FGPM beam, Composite Structures 182 (2017) 478–486. doi:10.1016/j.compstruct.2017.09.036.

[14] M. A. Trindade, A. Benjeddou, R. Ohayon, Piezoelectric active vibration control of damped sandwich beams, Journal of Sound and Vibration 246 (4) (2001) 653–677. doi:10.1006/jsvi.2001.3712.

[15] P. Bhattacharya, H. Suhail, P. K. Sinha, Finite element analysis and distributed control of laminated composite shells using LQR/IMSC approach, Aerospace Science and Technology 6 (4) (2002) 273–281. doi:10.1016/S1270-9638(02)01159-8.

[16] Z. Wang, Finite element modelling and LQG control of piezoelectric composite structure with distributed sensors and actuators, in: IEEE International Conference on Mechatronics and Automation (ICMA), IEEE, 2016, pp. 803–808. doi:10.1109/ICMA.2016.7558665.

[17] G. E. Stavroulakis, G. Foutsitzi, E. Hadjigeorgiou, D. Marinova, C. Baniotopoulos, Design and robust optimal control of smart beams with application on vibrations suppression, Advances in Engineering Software 36 (11) (2005) 806–813. doi:10.1016/j.advengsoft.2005.03.024.

[18] P. Shimon, E. Richer, Y. Hurmuzlu, Theoretical and experimental study of efficient control of vibrations in a clamped square plate, Journal of Sound and Vibration 282 (1) (2005) 453–473. doi:10.1016/j.jsv.2004.02.057.

[19] P. Shimon, Y. Hurmuzlu, A theoretical and experimental study of advanced control methods to suppress vibrations in a small square plate subject to temperature variations, Journal of Sound and Vibration 302 (3) (2007) 409–424. doi:10.1016/j.jsv.2005.01.054.

[20] X. Zhang, Z. Dong, M. Hromcik, K. Hengster-Movric, C. Faria, H. D. Van der Auweraer, W. Desmet, Reduced-order robust controller design for vibration reduction, Tech. Rep. 2016-01-1845, SAE Technical Paper (2016). doi:10.4271/2016-01-1845.

[21] W. H. Jee, C. W. Lee, H_∞ robust control of flexible manipulator vibration by using a piezoelectric-type servo-damper, Control Engineering Practice 2 (3) (1994) 421–430.

[22] K. Zhang, Mechatronic design under uncertainties, Ph.D. thesis, Ecully, Ecole centrale de Lyon (2013).

[23] W. Symens, H. Van Brussel, J. Swevers, Gain-scheduling control of machine tools with varying structural flexibility, CIRP Annals-Manufacturing Technology 53 (1) (2004) 321–324. doi:10.1016/S0007-8506(07)60707-0.

[24] B. Paijmans, W. Symens, H. Van Brussel, J. Swevers, A gain-scheduling-control technique for mechatronic systems with position-dependent dynamics, in: American Control Conference, IEEE, 2006, pp. 6–pp. doi:10.1109/ACC.2006.1657165.

[25] K. Zhou, J. C. Doyle, Essentials of robust control, Prentice hall Upper Saddle River, NJ, 1998.

[26] S. M. Han, H. Benaroya, T. Wei, Dynamics of transversely vibrating beams using four engineering theories, Journal of Sound and Vibration 225 (5) (1999) 935–988. doi:10.1006/jsvi.1999.2257.

[27] K. R. Kumar, S. Narayanan, Active vibration control of beams with optimal placement of piezoelectric sensor/actuator pairs, Smart Materials and Structures 17 (5) (2008) 055008. doi:10.1088/0964-1726/17/5/055008.

[28] M. Kant, A. P. Parameswaran, Modeling of low frequency dynamics of a smart system and its state feedback based active control, Mechanical Systems and Signal Processing 99 (2018) 774–789. doi:10.1016/j.ymssp.2017.07.018.

[29] R. W. Pryor, Multiphysics modeling using COMSOL: a first principles approach, Jones & Bartlett Publishers, 2009.

[30] T. P. Bohlin, Practical grey-box process identification: Theory and Applications, Springer Science & Business Media, London, 2006.

[31] P. WANG, G. Scorletti, A. Korniienko, M. Collet, Multi-variable model reduction of smart structure in active vibration control, 9th IFAC Symposium on Robust Control Design (ROCOND'18), Florianopolis, Brazil, 2018.

[32] V. Piefort, A. Preumont, Finite element modeling of piezoelectric structures, in: Samtech Users Conference, Paris, France, 2001.

[33] L. Meirovitch, Elements of vibration analysis, McGraw-Hill, New York, 1975.

[34] S. R. Moheimani, D. Halim, A. J. Fleming, Spatial control of vibration: theory and experiments, Vol. 10, World scientific, 2003.

[35] M. G. Singh, Handbook of large scale systems engineering applications, North Holland, North Holland, 1979.

[36] R. L. Williams, D. A. Lawrence, Linear state-space control systems, John Wiley & Sons, Hoboken, New Jersey, 2007. doi:10.1002/9780470117873.

[37] M. Safonov, R. Chiang, Model reduction for robust control: A schur relative error method, International Journal of Adaptive Control and Signal Processing 2 (4) (1988) 259–272. doi:10.1002/acs.4480020404.

[38] S. Boyd, L. El Ghaoui, E. Feron, V. Balakrishnan, Linear matrix inequalities in system and control theory, Vol. 15 of Studies in Applied Mathematics, SIAM, Philadelphia, PA, 1994. doi:10.1137/1.9781611970777.

[39] U. Mackenroth, Robust control systems: theory and case studies, Springer Science & Business Media, 2013. doi:10.1007/978-3-662-09775-5.

[40] C. Glader, G. Högnäs, P. Mäkilä, H. Toivonen, Approximation of delay systems—a case study, International Journal of Control 53 (2) (1991) 369–390. doi:10.1080/00207179108953623.

[41] U. Baur, P. Benner, L. Feng, Model order reduction for linear and nonlinear systems: A system-theoretic perspective, Archives of Computational Methods in Engineering 21 (4) (2014) 331–358. doi:10.1007/s11831-014-9111-2.

[42] D. Feliu-Talegon, A. San-Millan, V. Feliu-Batlle, Fractional-order integral resonant control of collocated smart structures, Control Engineering Practice 56 (2016) 210–223. doi:10.1016/j.conengprac.2016.07.016.

[43] H. Ji, J. Qiu, Y. Wu, J. Cheng, M. Ichchou, Novel approach of self-sensing actuation for active vibration control, Journal of Intelligent Material Systems and Structures 22 (5) (2011) 449–459.

[44] W. Gawronski, Advanced structural dynamics and active control of structures, Springer Science & Business Media, 2004. doi:10.1007/978-0-387-72133-0.

[45] A. Erturk, D. J. Inman, Piezoelectric Energy Harvesting, Wiley, UK, 2011. doi:10.1002/9781119991151.